

Combining cluster observables and stacked weak lensing to probe dark energy: Self-calibration of systematic uncertainties

Masamune Oguri¹ and Masahiro Takada²

¹*Division of Theoretical Astronomy, National Astronomical
Observatory of Japan, 2-21-1 Osawa, Mitaka, Tokyo 181-8588, Japan*

²*Institute for the Physics and Mathematics of the Universe (IPMU),
The University of Tokyo, Chiba 277-8582, Japan*

(Dated: March 20, 2019)

We develop a new method of combining cluster observables (number counts and cluster-cluster correlation functions) and stacked weak lensing signals of background galaxy shapes, both of which are available in a wide-field optical imaging survey. Assuming that the clusters have secure redshift estimates, we show that the joint experiment enables a self-calibration of important systematic errors inherent in these measurements, including the source redshift uncertainty and the cluster mass-observable relation, by adopting a *single* population of background source galaxies for the lensing analysis. The single source galaxy population allows us to use the relative strengths of the stacked lensing signals at different cluster redshifts for calibrating the source redshift uncertainty, which in turn leads to accurate measurements of the mean cluster mass in each redshift and mass bin. In addition, our formulation of the stacked lensing signals in Fourier space simplifies the Fisher matrix calculations, as well as the marginalization over the cluster off-centering effect which is one of the most significant uncertainties in the stacked lensing analysis. We show that upcoming wide-field surveys covering more than a few thousand square degrees yield stringent constraints on cosmological parameters including dark energy parameters, without any priors on nuisance parameters that model systematic uncertainties. Specifically, the stacked lensing information improves the dark energy figure of merit (FoM) by a factor of 4, compared to that from the cluster observables alone. The primordial non-Gaussianity parameter can also be constrained with a level of $\sigma(f_{\text{NL}}) \sim 10$. In this method, the mean source redshift is well calibrated to an accuracy of 0.1 in redshift, and the mean cluster mass in each bin to 5–10% accuracies, which demonstrates the success of the self-calibration of systematic uncertainties from the joint experiment.

I. INTRODUCTION

The abundance and its evolution of clusters of galaxies are thought to be one of main probes of cosmology including dark energy (e.g., [1]). This is because dark matter plays an essential role in the formation processes, indicating that the abundance and clustering properties of clusters can be predicted reasonably well by theory. In addition, the redshift evolutions of the cluster abundance and their clustering amplitudes are sensitive to the linear growth rate, which in turn is sensitive to the expansion history of the universe. In fact recent careful analyses of X-ray [2, 3] and optical [4] clusters have demonstrated that cluster abundance can provide useful constraints on cosmological parameters. In addition, clusters serve as powerful tests of non-standard cosmological scenarios including the modified theory of gravity [5–7] and primordial non-Gaussianity [8–12].

Perhaps the most significant challenge in cluster cosmology lies in the determination of masses for individual clusters or for a cluster sample as a whole. In many cases, we resort to mass-observable scaling relations, which have been calibrated by the intensive observations of (a subsample of) the clusters, in order to infer clusters masses. Popular choices of such observables include X-ray luminosities [13–15], X-ray temperatures [16–19], gas masses [20], optical richnesses [21], the Sunyaev-Zel’dovich (SZ) effect (the integrated gas pressure along the line-of-sight) [22, 23] and its X-ray analog [24–26]. However, it is not

an easy task to derive cluster masses observationally for calibrations, and moreover, we have to take account of its redshift evolution for robust cosmological studies.

Weak gravitational lensing provides a very powerful tool for measuring cluster masses. Gravitational lensing induces coherent tangential distortions of background galaxy shapes around a cluster, from which we can directly measure total mass profiles of the cluster (see [27] for a review). While accurate mass determinations with weak lensing are feasible only for massive clusters, by stacking signals from many clusters we can measure average masses of clusters down to less massive halos [20, 28–33]. This stacked lensing technique has indeed been applied to calibrate the mass-observable relation to derive interesting constraints on cosmological parameters (e.g., [4]). However, the stacked lensing analysis involves various systematic uncertainties. For instance, all weak lensing analysis is subject to the uncertainty in the redshift distribution of source galaxies used in the lensing analysis. In cosmic shear analysis, the estimation of source redshifts sometimes becomes the most significant source of systematic errors that challenge the use of weak lensing for cosmological studies [34–36]. In addition, one of the most significant uncertainties in stacked lensing analysis would be cluster centroiding (off-centering) errors which arises from the limitation of the mass centroid determination from available data [21, 37].

Clusters of galaxies are biased tracers of the underlying mass distribution. Thus one can obtain constraints

on the growth of structure from spatial clustering of massive clusters as well. Furthermore, the bias contains information on the cluster mass, which offers another opportunity to infer cluster masses in a statistical way. This opens up a possibility to calibrate the mass-observable relation from observing data themselves [38–40].

In this paper, we explore the potential of future optical cluster surveys, such as the Hyper Suprime-Cam (HSC) [41], Dark Energy Survey (DES) [42], and Large Synoptic Survey Telescope (LSST) [43], for constraining cosmological parameters. In these surveys, many clusters out to high-redshift ($z > 1$) will be identified in multi-color optical images, or with aid of Sunyaev-Zel'dovich (SZ) effects observed by Atacama Cosmology Telescope (ACT) [44, 45], South Pole Telescope (SPT) [46], or the all-sky Planck survey [98]. We combine number counts of these clusters with stacked weak lensing measurements, i.e., tangential shear profiles around the clusters taken in the stacking average. At small-scale the shear profiles constrain mean masses of cluster samples, whereas large-angle tangential shear profiles serve as a clean probe of halo-mass cross power spectrum. The cluster number counts and tangential shear profiles respectively contain important systematics, the mass-observable relation and the source redshift uncertainty. We show how the combination of these two observables can help self-calibrate these systematics to obtain robust constraints on cosmological parameters.

This paper is organized as follows. In Sec. II, we sketch out the basic idea of our technique, focusing on how we can overcome various difficulties inherent in cluster cosmology using the stacked weak lensing. We calculate the signals in Sec. III, and the covariance between observables in Sec. IV. We show results on the cosmological parameter forecast in Sec. V. We discuss possible systematics in Sec. VI, and conclude in Sec. VII. We choose the best-fit cosmological parameters from the seven-year Wilkinson Microwave Anisotropy Probe (WMAP) observations [47] as our fiducial cosmological model, with the matter density $\Omega_M = 0.266$, baryon density $\Omega_b = 0.04479$, the dark energy density $\Omega_{DE} = 0.734$ and its equation of state $w(a) = w_0 + (1 - a)w_a = -1$, the dimensionless Hubble constant $h = 0.710$, the power spectrum tilt $n_s = 0.963$, and the normalization of the power spectrum $\sigma_8 = 0.801$. Throughout the paper we assume a flat universe, i.e., $\Omega_M + \Omega_{DE} = 1$, and use the unit $c = 1$ for the speed of light.

II. BASIC IDEAS

The lensing distortion signal for a source galaxy in a particular direction θ on the sky and at redshift z_s is expressed as

$$\gamma(\theta; z_s) = 4\pi G \int_0^{z_s} dz a\chi(z) \left[1 - \frac{\chi(z)}{\chi(z_s)} \right] \Delta\Sigma(\chi\theta, z), \quad (1)$$

where $\chi = \chi(z)$ is the comoving angular diameter distance to redshift z , which is same as the comoving radial distance for a flat universe, $\Delta\Sigma$ denotes the mass distribution field along the line of sight, and the redshift is related to the scale factor a via $1 + z = 1/a$.

One of the most serious systematic errors in weak lensing is the photometric redshift error, i.e., uncertainty in estimating redshifts of source galaxies. Since a spectroscopic survey of all the source galaxies is observationally too expensive, in most cases redshifts of source galaxies have to be inferred based on their broadband photometries, the so-called photo- z information. For cosmic shear tomography [48–50], which is potentially the most powerful cosmological probe, future surveys need to calibrate mean redshifts of each tomographic bins to about 0.1% in order for constraints on cosmological parameters not to be significantly degraded [35]. This level of calibration is indeed very challenging.

In this paper, we propose a method which adopts the stacked lensing technique for the cosmological purpose, yet is insensitive to the photo- z errors. The key idea to overcome the source redshift uncertainty is to use a *single* population of background source galaxies to extract the lensing information, where source galaxies can be selected based on the photo- z information, in order to control and to calibrate its uncertainty.

More specifically, we consider the following situation. We study shear signals around a catalog of galaxy clusters, whose redshifts are assumed to be known either spectroscopically or photometrically. The photometric redshift estimate of each cluster is much more robust and accurate than photo- z estimates of individual galaxies, because photo- z estimates are more secure for early-type galaxies and photo- z uncertainties are statistically reduced by combining many member galaxies. We assume that redshifts of source galaxies are not overlapped with the cluster redshifts, i.e., all the source galaxies are located behind any clusters in the catalog. By cross-correlating the shapes of source galaxies with the cluster distribution in a particular redshift slice centered at z_l , we can measure the shear-cluster cross-correlation (or the stacked lensing signal) as a function of separation angles between the cluster center and the source galaxies:

$$\begin{aligned} \langle \gamma_+ \rangle(\theta; z_l) &\equiv \langle n_{\text{cluster}}(\theta'; z_l) \gamma_+(\theta - \theta') \rangle|_{z_s > z_{s,\min}} \\ &= 4\pi G(1 + z_l)^{-1} \chi_l \left[1 - \chi_l \left\langle \frac{1}{\chi(z_s)} \right\rangle \right] \langle \Delta\Sigma(\chi_l\theta, z_l) \rangle, \end{aligned} \quad (2)$$

where $\chi_l \equiv \chi(z_l)$ and

$$\left\langle \frac{1}{\chi(z_s)} \right\rangle \equiv \left[\int_{z_{s,\min}}^{\infty} dz_s \frac{dp}{dz_s} \frac{1}{\chi(z_s)} \right] \left[\int_{z_{s,\min}}^{\infty} dz_s \frac{dp}{dz_s} \right]^{-1}. \quad (3)$$

The redshift $z_{s,\min}$ denotes the minimum redshift used to define a source galaxy sample. The function $\langle \Delta\Sigma(\chi_l\theta, z_l) \rangle$ denotes the average mass profile around the lensing clusters at the redshift z_l , and dp/dz_s is the normalized redshift distribution of source galaxies defined so

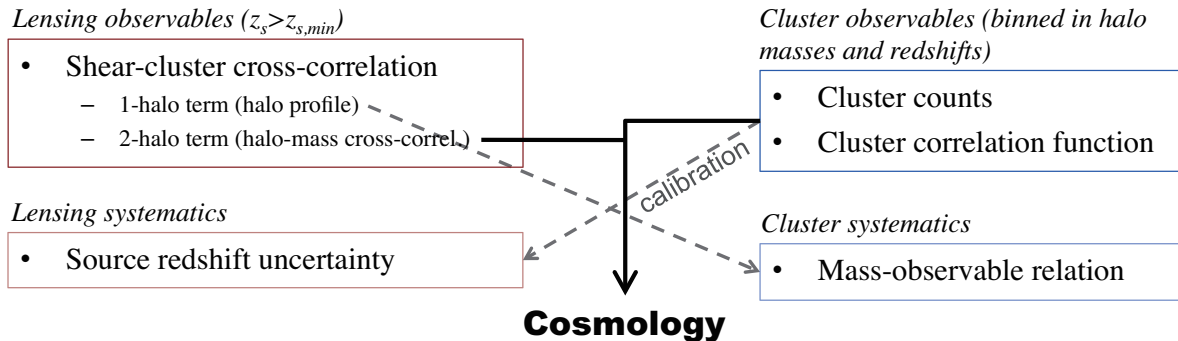


FIG. 1: A conceptual flow-chart of the method studied in this paper. We propose a joint experiment of combining the cluster observables and the shear-cluster correlation (or the so-called stacked lensing) to constrain cosmological parameters including dark energy parameters. The most serious systematic error inherent in each observable, the source redshift uncertainty and the mass-observable relation, can be calibrated out by combining the two observables (also see text around Eq. [2]). The cosmological power of this method arises mainly from the large-angle signals of the shear-cluster cross-correlation (2-halo term) and from the cluster observables. In addition, we consider how other systematic errors such as variations in the halo profile and the cluster centering offset affect cosmological constraints.

as to satisfy $\int_0^\infty dz_s dp/dz_s = 1$. Thus the dependence of the stacked lensing on source redshifts is only via a single quantity, the average $\langle \chi(z_s)^{-1} \rangle$ over the source galaxy population, and its effect is just to cause an offset in the overall amplitude of the stacked shear profile.

Eq. (2) indicates that the stacked lensing method in principle allows one to extract the lensing contribution at each cluster redshift from the total shear signals in source galaxy images. Thus, if cluster samples at different redshift slices are available as we study below, we can measure the redshift evolution of the stacked lensing signals, which provides a clue to the tomography of shear signals, i.e., how the shear signals in source galaxy images are built up over structures along the line of sight. A key in this step is that the stacked lensing signals at different redshifts all depend on the single quantity $\langle \chi(z_s)^{-1} \rangle$. Hence, even if the mean redshift of source galaxies is completely unknown as an extreme case, the quantity $\langle \chi(z_s)^{-1} \rangle$ can be self-calibrated by combining all the stacked lensing signals, as long as the stacked lensing signals at different cluster redshifts do not carry perfectly degenerate information.

On the other hand, the cluster observables (number counts of clusters and the cluster-cluster power spectrum) also involve several systematic uncertainties. The most important one is the uncertainty in the mass-observable relations. While the theoretical predictions for cluster observables are primarily given as a function of halo masses, the halo masses need to be inferred from the cluster observables, which causes uncertainties because of the imperfect relation between cluster observables and halo masses. Although previous studies have considered a possibility of calibrating the mass-observable relations by using clustering information of clusters (e.g., [38]), in our case cluster masses in each bin can directly be calibrated based on the stacked lensing signals at small

angular scales, which simply measures the mean mass profile of clusters (the 1-halo term).

Thus the weak lensing signals of distant galaxies and the cluster catalogs offer a promising synergy. Fig. 1 shows a conceptual flow-chart of the method studied in this paper. The combination of the two observables, the stacked lensing and the cluster observables, enables the self-calibration of the two major systematic errors, the source redshift uncertainty and the mass-observable relation. The cosmological power arises mainly from the large-angle signals of the stacked lensing as well as from the cluster observables, where both the observables are given as a function of different bins of cluster mass indicators (e.g., richnesses) and redshifts. In addition, we will carefully address other systematic errors that affect the lensing observables, such as variations in the cluster mass profile and the offset of cluster centers.

For a further clarity, the setup of the method is illustrated in Fig. 2. Unlike the conventional weak lensing tomography, we consider a single population of source galaxies defined so as not to be overlapped with clusters. We assume that redshifts of the clusters can be measured accurately, and clusters are divided into redshift bins. Since all cluster samples in different redshift bins share exactly the same source population, the bias in the source redshift distribution affects the shear signals in different redshift bins coherently in a way easily predicted by theory, which is the reason the source redshift uncertainty can be calibrated.

The self-calibration of the source redshift uncertainty and the mass-observable relations is feasible only when these two uncertainties are not completely degenerate. We check this point in Fig. 3. By increasing the source galaxy redshift, the stacked lensing signal at scales around the virial radius, $10'$ considered here, increases monotonically with increasing cluster redshift. Although

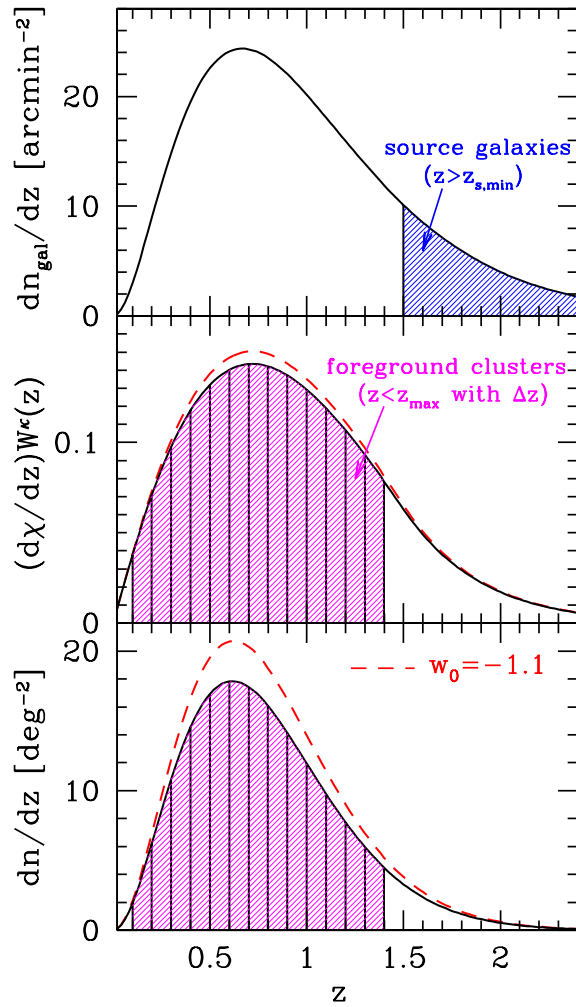


FIG. 2: The setup assumed in the paper. The population of source galaxies for weak lensing analysis is assumed to be located behind *any* clusters used for cosmological analysis (*top*). We study the cluster-shear cross correlation (whose signal is proportional to the lensing weight function $W^\kappa(z)$; *middle*) and the number of clusters as a function of cluster redshifts (*bottom*).

we can shift the mass of the cluster in a way to mimic this trend, the different mass dependence on the tangential shear at different radii suggests that we can break the degeneracy between the source redshift and the mass-observable relation by observing tangential shear signals over a wide range of radii. Furthermore, the trend is quite different from the changes of the tangential shear due to different dark energy equation of state, suggesting that these uncertainties are not degenerate with the uncertainty of cosmological parameters either.

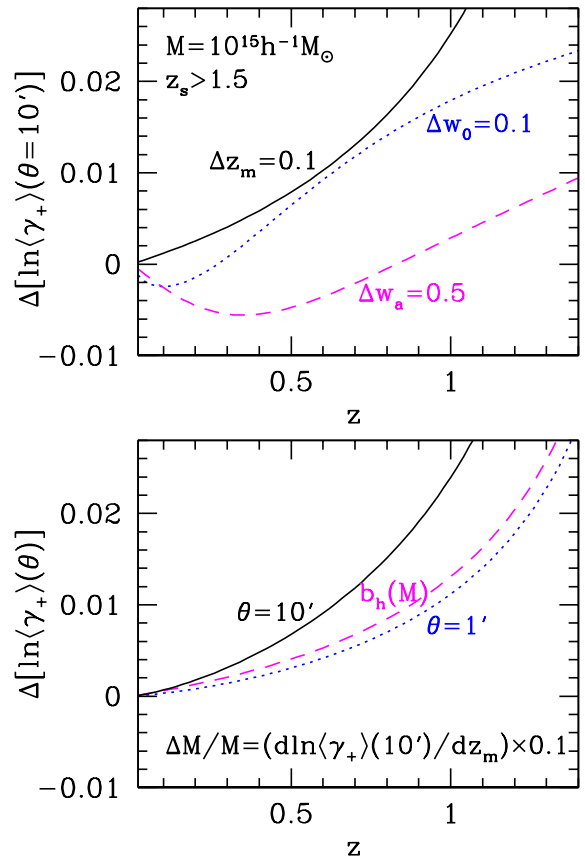


FIG. 3: *Upper panel*: The sensitivity of the tangential shear $\langle\gamma_+\rangle(\theta)$ at $\theta = 10'$ (roughly corresponding to the virial radius for a cluster with the mass $M = 10^{15} h^{-1} M_\odot$), as a function of the cluster redshift z . We show the fractional change of γ_+ by changing the mean redshift of the source galaxy distribution z_m (*solid*) and the dark energy equation of state w_0 (*dotted*) and w_a (*dashed*). See Sec. III for details of the setup and calculations. *Lower panel*: The change of $\langle\gamma_+\rangle(\theta)$ for different θ , when the mass of the cluster is shifted by $(d\ln\langle\gamma_+\rangle(10')/dz_m) \times 0.1$ in order to mimic the fractional change due to $\Delta z_m = 0.1$ (shown in the upper panel). The solid curve shows the fractional change of $\langle\gamma_+\rangle(\theta)$ at $\theta = 10'$, which indeed mimics the solid line in the top panel, whereas the dotted curve indicates the change at $\theta = 1'$. At $\theta \gg 10'$ the stacked lensing signal is dominated by the 2-halo term, whose mass dependence is simply the halo bias $b_h(M)$; the fractional change of $b_h(M)$ is shown by the dashed curve.

III. COSMOLOGICAL OBSERVABLES

A. A Flat Cold Dark Matter Model

Throughout this paper we work in the context within a spatially flat universe. The Hubble expansion rate, $H(z) \equiv (da/dt)/a$, is given by the scale factor $a(t)$ and is given in terms of energy density parameters as

$$H^2(a) = H_0^2 \left[\Omega_M a^{-3} + \Omega_{DE} e^{-3 \int_1^a da' (1+w(a'))/a'} \right], \quad (4)$$

where $H_0 = 100h \text{ km s}^{-1} \text{ Mpc}^{-1}$ is the present-day Hubble parameter. The parameter $w(a)$ specifies the equation of state for dark energy as $w(a) \equiv p_{\text{DE}}(a)/\rho_{\text{DE}}(a)$. Note that $\Omega_M + \Omega_{\text{DE}} = 1$ and we have used the convention $a(t_0) = 1$ today. The comoving angular diameter distance $\chi(z)$ is given as (note $1 + z = 1/a$),

$$\chi(z) = \int_0^z dz' \frac{1}{H(z')}, \quad (5)$$

which is related to the angular diameter distance $D_A(z)$ via $\chi(z) = (1+z)D_A(z)$.

Throughout this paper we adopt a parametrized form of the dark energy equation of state, $w(a) = w_0 + (1-a)w_a$. In this case, the Hubble expansion rate can be described as

$$H^2(a) = H_0^2 \left[\Omega_M a^{-3} + \Omega_{\text{DE}} a^{-3(1+w_0+w_a)} e^{-3w_a(1-a)} \right]. \quad (6)$$

Another important ingredient is the density fluctuation and its redshift evolution. In linear theory after matter-radiation equality, all Fourier modes of the mass density perturbation, $\delta(\mathbf{x}) (\equiv \delta\rho_m(\mathbf{x})/\bar{\rho}_m)$, grow at the same rate, the growth rate. For general dark energy equation of state $w(a)$, the growth rate $D(a)$ can be obtained by solving the following differential equation for $G(a) \equiv D(a)/a$ [51]

$$\frac{d^2 G}{d \ln a^2} + \left[\frac{5}{2} - \frac{3}{2} w(a) \Omega_{\text{DE}}(a) \right] \frac{dG}{d \ln a} + \frac{3}{2} [1 - w(a)] \Omega_{\text{DE}}(a) G = 0, \quad (7)$$

with the boundary condition $G(a) = 1$ and $dG/d \ln a = 0$ at $a \ll 1$. The linear density fluctuation is characterized by the linear power spectrum $P_m^L(k; z)$, which is related with the primordial curvature fluctuation as [52]

$$\frac{k^3}{2\pi^2} P_m^L(k; z) = \delta_\zeta^2 \left(\frac{2k^2}{5H_0^2 \Omega_M} \right)^2 [T(k)D(a)]^2 \times \left(\frac{k}{k_0} \right)^{n_s - 1 + (1/2)\alpha_s \ln(k/k_0)}, \quad (8)$$

where $T(k)$ is the transfer function of matter perturbations with baryon oscillations [53], δ_ζ is the normalization of the fluctuation at $k_0 = 0.002 \text{ Mpc}^{-1}$ following the convention in [54], and α_s is the running index of the primordial power spectrum. We adopt no running, i.e., $\alpha_s = 0$ as our fiducial choice.

B. Cluster Cosmology

The galaxy cluster observables we will consider in this paper are the number counts and the cluster power spectrum which can both be measured from a given survey region. In this section we briefly review the basics of the cluster observables.

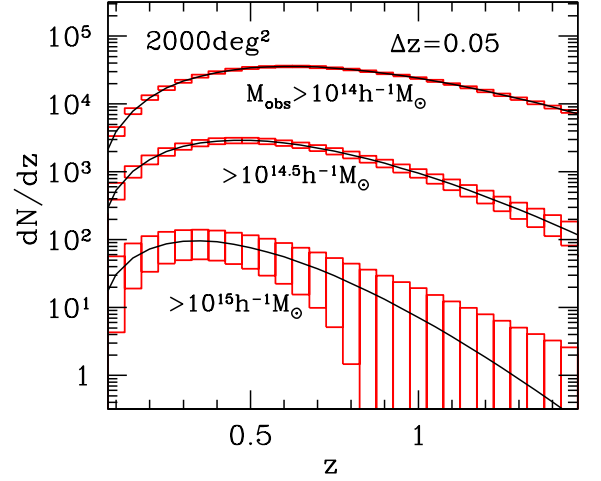


FIG. 4: The predicted number distributions dN/dz of clusters for the survey area of 2000 deg^2 . Here we consider three mass thresholds, $M_{\text{obs}} > 10^{14} h^{-1} M_\odot$, $10^{14.5} h^{-1} M_\odot$, and $10^{15} h^{-1} M_\odot$, where the observed mass M_{obs} is related with the true mass via Eq. (9). Boxes indicate the binned uncertainties (see Sec. IV A) for the bin size of $\Delta z = 0.05$.

1. Number Counts

The number counts of clusters in a given mass and redshift bin is the most fundamental quantity in cluster cosmology. The cosmological power of cluster number counts arises from their exponential sensitivity to the amplitude of the initial density perturbations. However, to implement this experiment, the total mass of each cluster, which is dominated by dark matter, has to be inferred from available observables such as lensing, member galaxies, X-ray and the SZ effect. We follow the previous work [40] to model the mass-observable relation including uncertainties in the mass inference from available data. The model relation assumes that the probability of obtaining the mass inferred from observables, M_{obs} , for a cluster with the true mass of M can be represented by the log-normal distribution:

$$p(M_{\text{obs}}|M) = \frac{1}{\sqrt{2\pi}\sigma_{\ln M}} \exp[-x^2(M_{\text{obs}})] \frac{1}{M_{\text{obs}}}, \quad (9)$$

where

$$x(M_{\text{obs}}) \equiv \frac{\ln M_{\text{obs}} - \ln M - \ln M_{\text{bias}}}{\sqrt{2}\sigma_{\ln M}}. \quad (10)$$

Unless otherwise specified, we assume $\ln M_{\text{bias}} = 0$ and $\sigma_{\ln M} = 0.3$, though uncertainties of the mass variance $\sigma_{\ln M}^2$ and the mass bias $\ln M_{\text{bias}}$, including their mass and redshift dependences, are fully taken into account in cosmological parameter forecasts.

The average number density of clusters that lie within the i -th redshift bin $z_{i,\text{min}} < z < z_{i,\text{max}}$ and the b -th mass bin defined in terms of the observed mass, $M_{b,\text{min}} <$

$M_{\text{obs}} < M_{b,\text{max}}$, is given by

$$\begin{aligned}\bar{n}_{i(b)} &= \int_{z_{i,\text{min}}}^{z_{i,\text{max}}} dz \frac{d^2V}{dzd\Omega} \int_{M_{b,\text{min}}}^{M_{b,\text{max}}} dM_{\text{obs}} \\ &\quad \times \int dM \frac{dn}{dM} p(M_{\text{obs}}|M) \\ &= \int dz \frac{d^2V}{dzd\Omega} \int dM \frac{dn}{dM} S_{i(b)}(M; z),\end{aligned}\quad (11)$$

where $d^2V/dzd\Omega = \chi^2/H(z)$ denotes the comoving volume element per unit redshift and per unit steradian, and $S_{i(b)}(M; z)$ is the selection function in the i -th redshift bin and the b -th mass bin, defined by

$$\begin{aligned}S_{i(b)}(M; z) &\equiv \Theta(z - z_{i,\text{min}})\Theta(z_{i,\text{max}} - z) \\ &\quad \times \frac{1}{2} [\text{erfc}\{x(M_{b,\text{min}})\} - \text{erfc}\{x(M_{b,\text{max}})\}],\end{aligned}\quad (12)$$

where $\Theta(x)$ is the Heaviside step function and $\text{erfc}(x)$ is the complementary error function. The redshift dependence of $S_{i(b)}(M)$ may come from a possible variation of the minimum and maximum mass with redshift, and also from a possible redshift evolution of $\ln M_{\text{bias}}$ and $\sigma_{\ln M}$ as considered later. In the following we will use the indices i, j, \dots and b, b', \dots to denote the redshift bins and the mass bins, respectively, for notational convenience.

The function dn/dM in Eq. (11) denotes the halo mass function, for which we employ a fitting formula presented by [55]. When we include the local-type primordial non-Gaussianity parametrized by f_{NL} , we employ the same method as adopted in [9] to compute the modified mass function.

For a given survey area of Ω_s the mean number counts of clusters in the redshift and mass bin is given by

$$N_{i(b)} = \Omega_s \bar{n}_{i(b)}. \quad (13)$$

We show in Fig. 4 how the number counts of clusters scale with redshift and mass threshold.

2. Cluster-Cluster Power Spectrum

Another useful cluster observable for cosmology is the cluster-cluster correlation function. While clusters are biased tracers of the underlying mass distribution, the cluster bias is, in contrast to the galaxy bias, well described by the halo bias. As in the case of the halo mass function, the halo bias is accurately predictable for a given cosmological model, e.g., based on a suite of N -body simulations, and is sensitive to halo mass. For this reason, combining the cluster number counts with the cluster correlation function can provide a promising way for self-calibrating the mass-observable relation [9, 11, 38–40]. Once the mass-observable relation is sufficiently calibrated, the cluster correlation function itself carries clean cosmological information in the sense that the information is mainly from the linear or weakly nonlinear

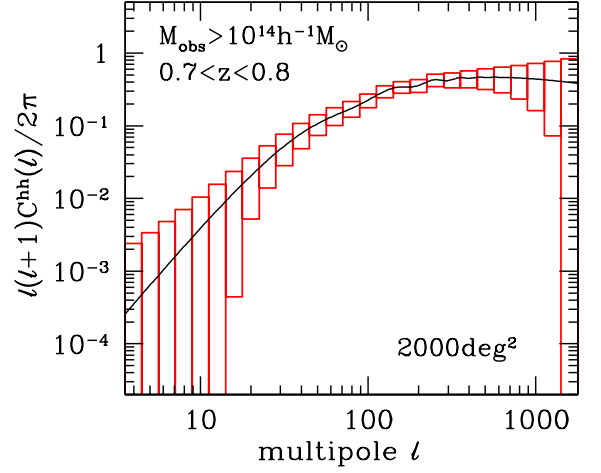


FIG. 5: The cluster-cluster angular power spectrum for clusters with $M_{\text{obs}} > 10^{14} h^{-1} M_{\odot}$ and $0.7 < z < 0.8$. Boxes indicate the binned uncertainties (see Sec. IV B) for the bin size of 0.1 dex, assuming the survey area of 2000 deg^2 .

regimes. Furthermore, if the primordial non-Gaussianity exists, it induces characteristic scale-dependent features on the halo bias at large length scales [8], which can be efficiently extracted by measuring the cluster correlation function.

In this paper we use the Fourier-counterpart of the cluster correlation function, the cluster power spectrum, for parameter forecasts. Using the Limber's approximation [56], we can compute the angular power spectrum between pairs of clusters, which are in the b - and b' -th mass bins, respectively, and at the same i -th redshift bin:

$$C_{i(bb')}^{\text{hh}}(\ell) = \int d\chi W_{i(b)}^{\text{h}}(z) W_{i(b')}^{\text{h}}(z) \chi^{-2} P_m^{\text{L}}\left(k = \frac{\ell}{\chi}; z\right), \quad (14)$$

where $P_m^{\text{L}}(k; z)$ is the linear mass power spectrum at redshift z (Eq. [8]), and $W_{i(b)}^{\text{h}}$ is the weight function defined as

$$W_{i(b)}^{\text{h}}(z) \equiv \frac{1}{\bar{n}_{i(b)}} \frac{d^2V}{d\chi d\Omega} \int dM \frac{dn}{dM} S_{i(b)}(M) b_h(M; z). \quad (15)$$

Here $d^2V/d\chi d\Omega = \chi^2$ and $b_h(M; z)$ is the bias parameter for halos with mass M and at redshift z , which should not be confused with the mass bin index (b). Again, we adopt a fitting formula presented by [55] in computing $b_h(M; z)$. When we include the effect of the primordial non-Gaussianity on the halo bias, we employ the method [8, 57].

Fig. 5 shows an example of the angular power spectrum, for clusters in a redshift slice of $0.7 < z < 0.8$ and with observed masses $M_{\text{obs}} > 10^{14} h^{-1} M_{\odot}$. The boxes around the curve show the expected measurement errors for our fiducial survey (see below for details).

C. Weak Lensing Observables

1. Weak Lensing Basics

Due to the geometrical nature of gravitational lensing, the lensing shear amplitude scales with the critical surface density Σ_{crit} for a given population of source galaxies

$$\Sigma_{\text{crit}}^{-1}(z) \equiv 4\pi G\chi(z)(1+z)^{-1} \left[1 - \chi(z) \left\langle \frac{1}{\chi(z_s)} \right\rangle \right], \quad (16)$$

where $\langle \chi(z_s)^{-1} \rangle$ is the inverse distance averaged over the source galaxy population defined by $z_s > z_{s,\text{min}}$ (see Eq. [3]). Since we are interested in the statistical weak lensing, we here defined the *mean* critical surface density for a lensing object at redshift z , averaged over the redshift distribution of source galaxies as in Eq. (2).

To compute the lensing efficiency, we need to specify a population of source galaxies. We simply assume that photometric galaxies follow the redshift distribution given by

$$\frac{dp}{dz_s} = \frac{z_s^2}{2z_0^3} \exp\left(-\frac{z_s}{z_0}\right), \quad (17)$$

where z_0 is free parameter, and dp/dz_s satisfies the normalization condition $\int_0^\infty dz_s dp/dz_s = 1$. With this form, the mean redshift z_m is given as $z_m = \langle z_s \rangle = 3z_0$. As our fiducial choice, we assume $z_0 = 1/3$ corresponding to the mean redshift $z_m = 1$, which roughly mimics the depth of the Subaru Hyper Suprime-cam (HSC) Survey.

For the method studied in this paper, we focus on a sub-population of source galaxies for extracting the lensing signals (see also Sec. II for detailed discussions). The source galaxies are defined from galaxies at redshifts greater than the minimum redshift $z_{s,\text{min}}$. Our fiducial choice is $z_{s,\text{min}} = 1.5$ such that source galaxies are behind all clusters of interest. Thus the source redshift dependence of the lensing efficiency is only via the single quantity, $\langle \chi_s^{-1} \rangle$. We will employ the mean source redshift of the whole galaxy distribution (i.e., *not* the mean redshift of the sub-population defined by $z_s > z_{s,\text{min}}$), z_m , to describe the source redshift dependence in making parameter forecasts.

The lensing shearing effect on source galaxy images is caused by the foreground structure along the line of sight. The shear amplitude for a given galaxy in the angular direction θ on the sky is closely related to the weighted mass density field along the line of sight (e.g., see [27])

$$\vec{\gamma}(\theta) \leftarrow \kappa(\theta) \equiv \int d\chi W^\kappa(z) \delta_m(\chi\theta, \chi), \quad (18)$$

where the vector notation $\vec{\gamma}$ is used to explicitly show that the shear field is a spin-2 field, i.e., has two components at each position on the sky, κ is the so-called convergence field, and $\delta_m(\chi\theta, \chi)$ is the mass density fluctuation field.

Note that lensing does not occur for a completely homogeneous universe with $\delta_m = 0$. The function $W^\kappa(z)$ is the lensing weight function defined by

$$W^\kappa(z) \equiv \frac{\bar{\rho}_m(z)}{(1+z)\Sigma_{\text{crit}}(z)}, \quad (19)$$

where $\bar{\rho}_m(z)$ denotes the mean mass density of the universe at redshift z .

Using the Limber's approximation, we can compute the lensing power spectrum for the source galaxy population defined above as

$$C^{\kappa\kappa}(\ell) = \int d\chi [W^\kappa(z)]^2 \chi^{-2} P_m^{\text{NL}}\left(k = \frac{\ell}{\chi}; z\right), \quad (20)$$

where $P_m^{\text{NL}}(k)$ denotes the nonlinear mass power spectrum. We use the fitting formula in [58] for computing $P_m^{\text{NL}}(k)$ for a given cosmological model.

2. Shear-Cluster Power Spectrum: Stacked Lensing

As briefly described in Sec. II, if a catalog of galaxy clusters in the similar redshift range is available, the contribution of the clusters to the lensing signals of background source galaxies can be extracted by measuring a cross-correlation between the cluster distribution and the shapes of source galaxies – the so-called shear-cluster correlation or the stacked lensing. For the limit that a redshift slice of clusters, centered at z_l , is sufficiently thin, the shear-cluster correlation is given by

$$\langle \gamma_+ \rangle(\theta; z_l) \equiv \frac{1}{\bar{n}_{\text{cl}}} \langle n_{\text{cl}}(\theta'; z_l) \gamma_+(\theta - \theta') \rangle = \frac{\Delta\Sigma_m(\chi_l\theta; z_l)}{\Sigma_{\text{crit}}(z_l)}, \quad (21)$$

where $\chi_l \equiv \chi(z_l)$ and $\Delta\Sigma_m(\chi_l\theta; z_l)$ is the radial profile of the projected mass density around the cluster center. Observationally the shear-cluster correlation can be measured by averaging the tangential ellipticity component of source galaxy images in each radial bins over all the pairs of background galaxies and clusters in the sample, where the tangential ellipticity is defined with respect to the cluster center in each cluster region [20, 30, 32]. Note that the cluster distribution is treated as discrete, point distribution, and a representative point for each cluster needs to be chosen for each cluster, the cluster center in this method [59].

There are notable advantages in the stacked lensing technique, e.g., compared to cosmic shear. (1) As discussed at length in Sec. II, the source redshift uncertainty can be calibrated by combining the stacked lensing signals of different cluster redshifts. (2) The stacked lensing profile is less sensitive to substructures within and asphericity of the individual clusters and also to uncorrelated large-scale structure along the same line of sight. Since the signal probed is linear in shear, which can be both positive and negative due to its spin-2 field nature, these contaminating effects are averaged out via

the stacking, if a sufficient number of clusters are available and as long as the universe is statistically isotropic and homogeneous. As a result, the stacked lensing technique probes the *average* mass distribution around the clusters, which can be considered as a spherically symmetric profile. Therefore the stacked lensing profile is one-dimensional, i.e., given as a function of radius from the cluster center. (3) The stacking boosts the signal to noise ratios of shear signals at very large radii, where the shear detection is limited by too small signal for an individual cluster. The large-angle shear signal is in the linear or weakly nonlinear regime, and hence carries relatively clean cosmological signals. (4) If source galaxies are not overlapped with cluster redshifts, another serious contamination to cosmic shear, the intrinsic ellipticity alignment [60], does not affect the stacked lensing signals.

Assuming the flat-sky approximation, we can express the stacked lensing profile in terms of the angular power spectrum $C_{i(b)}^{\text{h}\kappa}(\ell)$ as

$$\langle \gamma_+ \rangle_{i(b)}(\theta) = \int \frac{\ell d\ell}{2\pi} C_{i(b)}^{\text{h}\kappa}(\ell) J_2(\ell\theta), \quad (22)$$

where $J_2(x)$ is the second-order Bessel function. The full-sky expression can be recently formulated in [61], where it was shown that the effect of the celestial sphere causes only a few percent change in the shear amplitude at very large angles greater than 10 degrees. We do not think that the inaccuracy of the flat-sky approximation largely changes the following results, but a more rigorous calculation will be our future work. The angular power spectrum contains the equivalent information to the stacked lensing profile. Hence we will use the power spectrum in conducting parameter forecasts for computational simplicity. For example, the covariance calculation is easier in Fourier space than in real space.

The stacked shear profile arises from two contributions. The shear signal at angular scales smaller than a typical projected virial radius of clusters arises from the average mass distribution within one halo, the so-called 1-halo term, while the large-angle shear arises from the average large-scale structure surrounding the clusters, the 2-halo term. In what follows, we model the shear-cluster correlation function based on the halo model.

3. Stacked Lensing: 1-Halo Term

As described above, we need a model of the radial mass profile of halo in order to compute the 1-halo term at small angular scales. In this paper, we employ the Navarro-Frenk-White (NFW) profile [62] as used in [59]. The NFW profile is defined by

$$\rho(r) = \frac{\rho_s}{(r/r_s)(1+r/r_s)^2}. \quad (23)$$

The density parameter ρ_s is specified by imposing that the mass enclosed within a sphere of the virial radius is

equal to the virial mass M

$$\rho_s = \frac{\Delta(z)\bar{\rho}_m(z)c^3}{3m_{\text{nfw}}(c)} = \frac{M}{4\pi r_s^3 m_{\text{nfw}}(c)}, \quad (24)$$

where

$$m_{\text{nfw}}(c) \equiv \int_0^c \frac{r}{(1+r)^2} dr = \ln(1+c) - \frac{c}{1+c}. \quad (25)$$

Here $c \equiv r_{\text{vir}}/r_s$ is a concentration parameter, $\Delta(z)$ is a nonlinear overdensity that defines the virial mass based on the spherical collapse model (we adopt a fitting formula by [63]). Motivated by the result of N -body simulations (e.g., [64]), we adopt the following model for the mass and redshift dependence of the concentration parameter

$$c(M, z) = A_{\text{vir}} \left(\frac{M}{2 \times 10^{12} h^{-1} M_{\odot}} \right)^{B_{\text{vir}}} (1+z)^{C_{\text{vir}}}, \quad (26)$$

Here A_{vir} , B_{vir} and C_{vir} are free parameters, and we will employ $(A_{\text{vir}}, B_{\text{vir}}, C_{\text{vir}}) = (7.85, -0.081, -0.71)$ as our fiducial parameter set according to the result in [65].

Using the method developed in [33] (also see [59]), the Limber's approximation and the flat-sky approximation, we can derive the power spectrum for the 1-halo term of shear-cluster correlation between the source galaxies and the clusters in the i -th redshift slice and the b -th mass bin. We find that the 1-halo term is described by

$$C_{i(b)}^{\text{h}\kappa, 1\text{h}}(\ell) = \frac{1}{\bar{n}_{i(b)}} \int dz \frac{d^2 V}{dz d\Omega} \times \int dM \frac{dn}{dM} S_{i(b)}(M; z) \tilde{\kappa}_M(\ell; z), \quad (27)$$

where $\tilde{\kappa}_M(\ell)$ denotes the two-dimensional Fourier transform of the projected NFW profile (i.e., convergence $\kappa(\theta)$) defined as

$$\tilde{\kappa}_M(\ell; z) \equiv \int 2\pi\theta d\theta \kappa(\theta) J_0(\ell\theta) = \frac{M \tilde{u}_M(k = \ell/\chi; z)}{(1+z)^{-2} \chi^2 \Sigma_{\text{crit}}(z)}. \quad (28)$$

Here $J_0(x)$ is the zeroth order Bessel function and $\tilde{u}_M(k)$ denotes the three-dimensional Fourier transform of the normalized NFW profile $u_M(r) = \rho(r)/M$, which has the following analytic form [66]

$$\tilde{u}_M(k) = \frac{1}{m_{\text{nfw}}(c)} [\sin x \{ \text{Si}[x(1+c)] - \text{Si}(x) \} + \cos x \{ \text{Ci}[x(1+c)] - \text{Ci}(x) \} - \frac{\sin(xc)}{x(1+c)}], \quad (29)$$

where $x \equiv (1+z)kr_s$, and $\text{Si}(x)$ and $\text{Ci}(x)$ are sine and cosine integrals. The relation between the two-dimensional and three-dimensional Fourier transforms of halo profile was also discussed in Sec. 3.2 in [67].

4. Effect of Halo Centering Offset

For the derivation of the 1-halo term above, we implicitly assume that the stacking can be done by properly selecting the halo center of each cluster, e.g., the Fourier transform of halo profile, $\tilde{u}_M(k)$ (Eq. [29]), is defined with respect to the halo center. On individual cluster basis, a dark matter halo generally contains many substructures, has a non-spherically symmetric mass distribution, and has no clear boundary with its surrounding structures, all of which reflect the collision-less nature of dark matter. Such a complexity, as well as invisible nature of dark matter, implies that it is not straightforward to define the halo center for each cluster. Observationally the cluster center will be chosen from either/both of the position of brightest cluster galaxy (BCG) or the peak of the X-ray or SZ maps. If the significant strong/weak lensing detection is achieved, albeit rare, the cluster center can be inferred from the mass distribution reconstructed from the lensing. Recently we [68] found that, from the detailed weak lensing analysis of individual clusters, the BCG position is indeed close to the center inferred from the lensing-reconstructed mass distribution, although there are some clusters whose centers appear to be significantly offset from their BCGs. In what follows, we develop a formulation to account for the effect of possible centering offset on the stacked lensing.

As derived in detail in Appendix A, the halo centering offset acts as a smoothing effect on the stacked lensing signal. For a spherically symmetric halo (in an average sense), if the halo center is incorrectly chosen with an offset angle θ_{off} from the true center, the measured stacked lensing profile in Fourier space is modified as

$$\tilde{\kappa}_{M,\text{off}}(\ell) = \tilde{\kappa}_M(\ell) J_0(\ell \theta_{\text{off}}). \quad (30)$$

In this paper, we are interested in the statistical average of tangential shears around many different clusters. Naturally all clusters do not share the same offset angle, but rather the offset should follow some probability distribution

$$\tilde{\kappa}_{M,\text{off}}(\ell) = \tilde{\kappa}_M(\ell) \int d\theta_{\text{off}} J_0(\ell \theta_{\text{off}}) p_{\text{off}}(\theta_{\text{off}}), \quad (31)$$

where $p(\theta_{\text{off}})$ is the probability distribution function of θ_{off} .

As implied from the mock galaxy catalog [21] or lensing measurements [68], one reasonable choice of $p_{\text{off}}(\theta_{\text{off}})$ is a sum of the two-dimensional Gaussian distributions given by

$$p_{\text{off}}(\theta_0) = \sum_i f_i \frac{\theta_0}{\sigma_{s,i}^2} \exp\left(-\frac{\theta_0^2}{2\sigma_{s,i}^2}\right). \quad (32)$$

In this case, we can analytically integrate Eq. (31) to obtain

$$\tilde{\kappa}_{M,\text{off}}(\ell) = \tilde{\kappa}_M(\ell) \sum_i f_i \exp\left(-\frac{1}{2}\sigma_{s,i}^2 \ell^2\right), \quad (33)$$

where σ_s denotes the width of the Gaussian distribution in radian. Again the distribution of the offset angles has been explored by studying individual clusters based on both numerical simulations [21, 69] and observations [68, 70–72]. Motivated by the results of such previous works, in this paper, we adopt a two-component model consisting of clusters whose inferred center align well with the true center and clusters with their measured center significantly offset from the true center. Specifically, we adopt the following expression:

$$\tilde{\kappa}_{M,\text{off}}(\ell) = \tilde{\kappa}_M(\ell) \left[f_{\text{cen}} + (1 - f_{\text{cen}}) \exp\left(-\frac{1}{2}\sigma_s^2 \ell^2\right) \right], \quad (34)$$

with f_{cen} denotes a parameter to specify the fraction of clusters which have their inferred center to be consistent with the true center. We employ $f_{\text{cen}} = 0.75 + 0.05 \ln(M/M_{\text{piv}})$ with $M_{\text{piv}} = 3 \times 10^{14} h^{-1} M_{\odot}$ and $D_A(z)\sigma_s = 0.42 h^{-1} \text{Mpc}$ as our fiducial values, which are roughly consistent with the results obtained from mock galaxy catalogs [21].

Thus the 1-halo term of the shear-cluster power spectrum including the halo off-centering effect can be computed by replacing $\tilde{\kappa}_M(\ell)$ in Eq. (27) with $\tilde{\kappa}_{M,\text{off}}(\ell)$ in Eq. (34) for a given model of the halo centering offsets. The real-space stacked lensing profile can be also obtained via the transform given by Eq. (22).

Fig. 6 shows the expected signals for the 1-halo term of the stacked lensing profile, with and without the effect of halo centering offset (see Fig. 4 in [21] for the similar plot). Here we consider lensing clusters with observed masses $M_{\text{obs}} > 10^{14} h^{-1} M_{\odot}$ and in the redshift slice of $0.7 < z < 0.8$. The figure explicitly shows that the halo off-centering effect smooths out the stacked lensing signal at small angular scales. In other words, for a fixed sample of clusters, a better choice of the cluster center can be explored to some extent by monitoring the shear amplitudes in order to maximize the shear amplitudes at small radii. At least, if several choices of the cluster center are available, e.g., from optical, X-ray and SZ data, the stacked lensing amplitudes can be compared to obtain the best inference of the cluster center for stacked lensing analysis.

D. Stacked Lensing: 2-Halo Term

Now we consider the 2-halo term contribution to the stacked lensing signal, which arises from the mass distribution surrounding lensing clusters. Again by employing the halo model formulation (e.g., [59]), we can derive the 2-halo term of power spectrum for the stacked lensing between the source galaxies and the clusters in the i -th redshift bin and the b -th mass bin as

$$C_{i(b)}^{\text{h}\kappa, 2\text{h}}(\ell) = \int d\chi W_{i(b)}^{\text{h}}(z) W^{\kappa}(z) \chi^{-2} P_m^{\text{L}}\left(k = \frac{\ell}{\chi}; z\right), \quad (35)$$

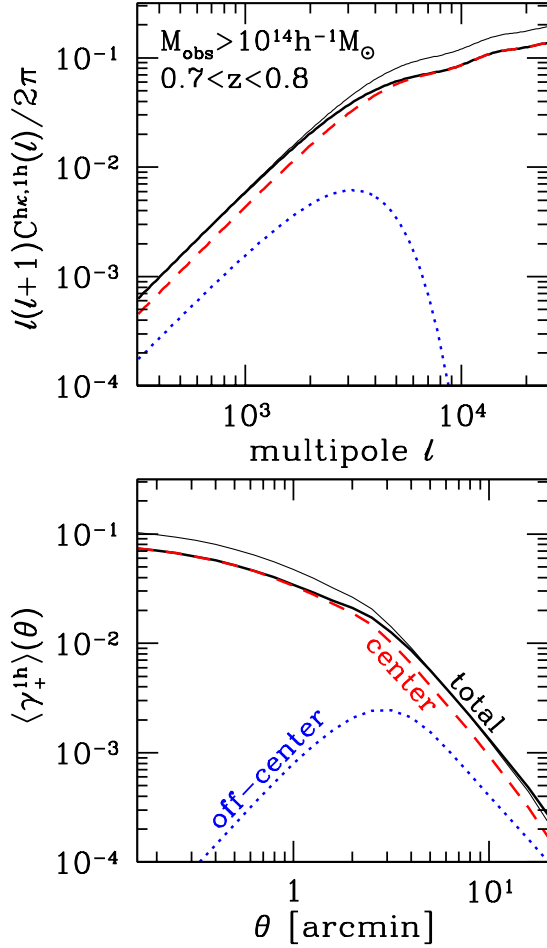


FIG. 6: *Upper panel:* The angular power spectrum of stacked cluster weak lensing signals from main halos (1-halo term) with the effect of off-centering. In this example we consider clusters with $M_{\text{obs}} > 10^{14} h^{-1} M_{\odot}$ located as $0.7 < z < 0.8$. The total power spectrum is shown by the thick solid curve, whereas the contributions from populations with and without off-centering effect, as expressed by Eq. (34), are shown by the dotted and dashed curves, respectively. The thin solid curve shows the total power spectrum when the true centers of all the clusters are properly identified (i.e., $f_{\text{cen}} = 1$). *Lower panel:* The corresponding stacked shear profiles in real space.

where the weight functions $W^{\text{h}}(z)$ and $W^{\kappa}(z)$ are given by Eqs. (15) and (19), respectively. We have set $\int dM (dn/dM) b(M) M \tilde{u}_M(k) = 1$ at angular scales relevant for the 2-halo term; the prefactor appears in the formal derivation of 2-halo term based on the halo model formulation (see [59]), but we used the expression above for notational simplicity. We have checked that this simplification does not change the following results.

1. Summary: Halo Model Calculation of Stacked Lensing

In summary, using Eqs. (27), (34), and (35), we can compute the halo model based prediction for the angular power spectrum of the stacked lensing for a given cosmological model:

$$C_{i(b)}^{\text{h}\kappa}(\ell) = C_{i(b)}^{\text{h}\kappa,1\text{h}}(\ell) + C_{i(b)}^{\text{h}\kappa,2\text{h}}(\ell). \quad (36)$$

The corresponding stacked shear profile in real space is computed using Eq. (22).

Fig. 7 shows the expected stacked lensing signals in both Fourier and real spaces, for several different redshift slices. The figure shows that the 1-halo term arising from the halo mass profile dominates the signal at small angular scales $\lesssim 10'$ or multipoles greater than a few hundred, while the 2-halo term dominates at large scale, $\ell \lesssim 10^3$ or $\theta \gtrsim 10'$. The boxes around each curve show the expected 1σ measurement errors in each angular or multipole bins for a Subaru HSC-type weak lensing survey with an area coverage of 2000 deg^2 , which are computed using the covariance matrix calculations shown in the next section. Note that the error bars are uncorrelated between different multipole bins for the power spectrum measurement under the Gaussian error assumption, which we will throughout this paper assume, while the error bars are highly correlated for the real-space stacked shear measurement.

IV. COVARIANCES OF OBSERVABLES AND FISHER MATRICES

To estimate the accuracies of parameter estimation for a given survey, we employ the Fisher matrix formalism. In this method we first need to quantify the measurement errors of cosmological observables for given survey parameters that are chosen to resemble planned surveys. The covariance matrices of the observables can model the measurement errors. Then we can propagate the measurement errors into uncertainties of parameter estimation using the Fisher matrix formalism. In this section, we present the covariances between the observables defined in Sec. III, and define the Fisher matrices of each observables.

A. Number Counts

The covariance matrix of cluster number counts (Eq. [13]) is given by [59, 73]

$$\text{Cov}(N_{i(b)}, N_{j(b')}) = N_{i(b)} \delta_{ij}^K \delta_{bb'}^K + S_{i(bb')} \delta_{ij}^K, \quad (37)$$

where δ_{ij}^K denotes the Kronecker delta function; $\delta_{ij}^K = 1$ if $i = j$, otherwise $\delta_{ij}^K = 0$. The first term of Eq. (37) denotes the shot noise arising due to the finite number of clusters available, and is only non-vanishing when both

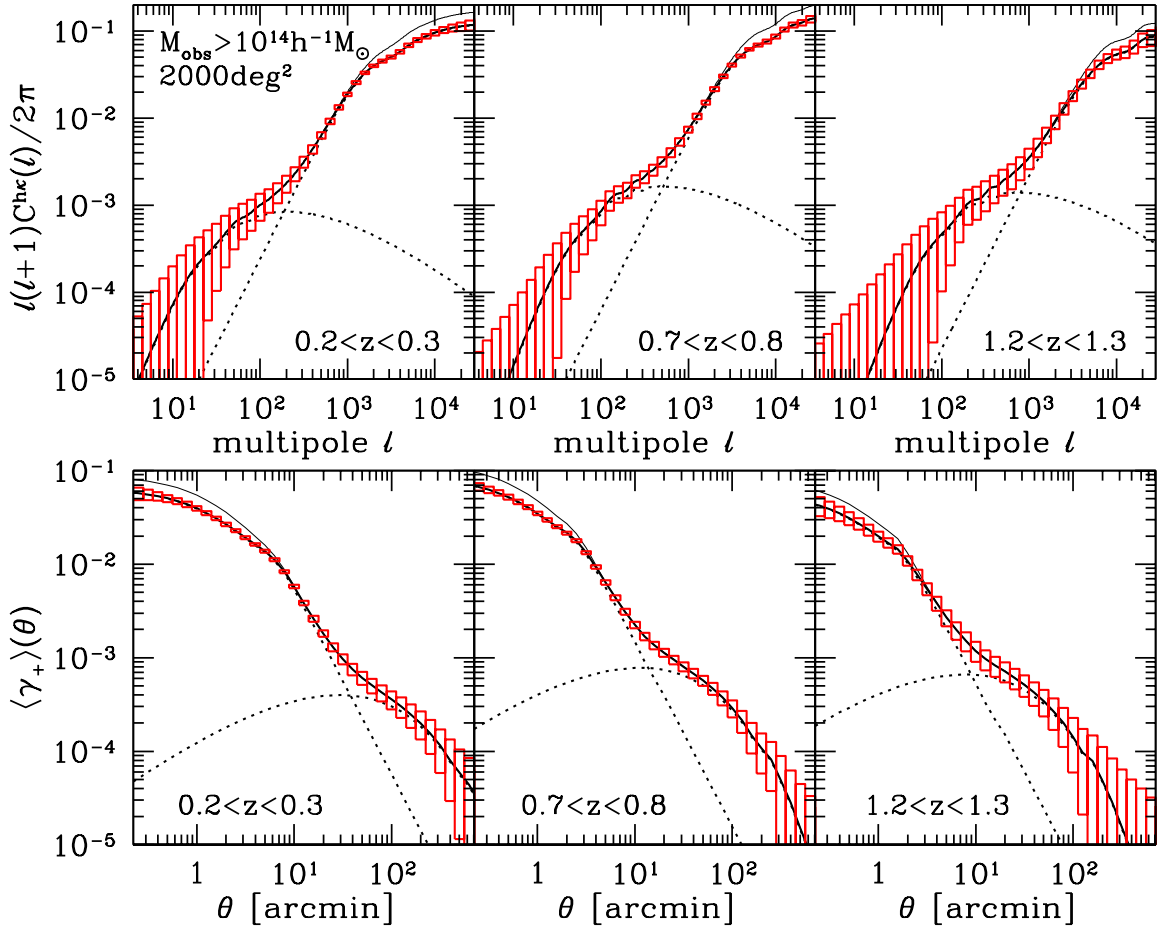


FIG. 7: The stacked lensing signals in Fourier (*upper-row panels*) and real (*lower panels*) spaces, for three cluster redshift slices, $0.2 < z < 0.3$ (*left panel*), $0.7 < z < 0.8$ (*middle*), and $1.2 < z < 1.3$ (*right*), respectively. Note that in all the plots we assumed a background source galaxy sample defined by $z_s > 1.5$. The dotted curves indicate the contributions from 1-halo and 2-halo terms. While the effect of off-centering is included assuming the two component model described by Eq. (34), we also show the case without any offset by the thin solid curves for reference. The boxes around each curve indicate the measurement errors for the binned power spectra or the binned shear profiles (see Sec. IV B) for the bin size of 0.1 dex, assuming the survey area of 2000 deg^2 .

the redshift bins and the mass bins are same, $i = j$ and $b = b'$. On the other hand, the second term of Eq. (37) gives the sampling variance contribution, which arises because the number of clusters is fluctuated according to the large-scale modes of large-scale structure within a surveyed region:

$$S_{i(bb')} \equiv \Omega_s^2 \bar{n}_{i(b)} \bar{n}_{i(b')} \int d\chi W_{i(b)}^h(z) W_{i(b')}^h(z) \chi^{-2} \times \int \frac{\ell d\ell}{2\pi} \left| \tilde{W}_s(\ell \Theta_s) \right|^2 P_m^L \left(k = \frac{\ell}{\chi}; z \right). \quad (38)$$

Here $\tilde{W}_s(\ell)$ being the Fourier transform of the survey window function. We assume a circular survey geometry with survey area $\Omega_s = \pi \Theta_s^2$ for simplicity, with the resulting survey window function of $\tilde{W}_s(\ell) = 2J_1(\ell \Theta_s)/(\ell \Theta_s)$. The Kronecker delta δ_{ij}^K in the second term of Eq. (37) imposes that the sampling variance is vanishing for the

counts of different redshift slices, i.e. $i \neq j$, assuming that the redshift slices of clusters are sufficiently wide such that the cluster distributions in different redshift slices are uncorrelated.

Then we can write the Fisher matrix for the cluster number counts $\mathbf{N} (\equiv N_{i(b)})$ as

$$F_{\alpha\beta}^N = \sum_{I,J} \frac{\partial \mathbf{N}_I}{\partial p_\alpha} [\text{Cov}(\mathbf{N}, \mathbf{N})]_{IJ}^{-1} \frac{\partial \mathbf{N}_J}{\partial p_\beta}, \quad (39)$$

where the indices I, J run over the cluster redshift and mass bins (i, b) and p_α denotes a set of model parameters.

B. Power Spectrum Observables

1. Covariance Matrices and Fisher Matrix

The angular power spectra we consider in this paper as observables are the cluster power spectrum and the shear-cluster power spectrum (note that we will also study how the result is changed by further adding the cosmic shear power spectrum). Therefore the data vector can be given as

$$\mathbf{D} \equiv \left(C_{i(bb')}^{\text{hh}}, C_{i(b)}^{\text{h}\kappa} \right). \quad (40)$$

We need to model the auto- and cross-covariances of these elements.

There are two contributions to the sampling variance in the power spectrum covariance, the Gaussian and non-Gaussian error contributions, where the later arises from nonlinear clustering of structure formation. In this paper we ignore the non-Gaussian error covariances for simplicity. As carefully studied in [74] (also see [75] for a simulation based study), the non-Gaussian errors are significant at small angular scales, although the impact on parameter estimation is not large as long as a sufficient set of cosmological parameters is included. For example, for the case of cosmic shear power spectrum, the non-Gaussian errors degrade the *marginalized* error of each parameter only by about 10%. This also likely holds for the case of shear-cluster power spectrum combined with the cluster experiments, although a confirmation of this assumption needs to be carefully studied.

Thus, assuming the Gaussian error covariance, the covariance matrix of the shear-cluster power spectrum is given by

$$\begin{aligned} \text{Cov}\left(C_{i(b)}^{\text{h}\kappa}, C_{j(b')}^{\text{h}\kappa}\right) &= \frac{4\pi}{\Omega_s} \frac{\delta_{\ell\ell'}^K}{(2\ell+1)\Delta\ell} \\ &\times \left[\hat{C}_{i(bb')}^{\text{hh}} \hat{C}^{\kappa\kappa} \delta_{ij}^K + C_{i(b)}^{\text{h}\kappa} C_{j(b')}^{\text{h}\kappa} \right]. \end{aligned} \quad (41)$$

The spectra $\hat{C}^{\kappa\kappa}$ and $\hat{C}_{i(bb')}^{\text{hh}}$ are the observed power spectra including the shot noise contamination

$$\hat{C}_{i(bb')}^{\text{hh}} \equiv C_{i(bb')}^{\text{hh}} + \frac{1}{\bar{n}_{i(b)}} \delta_{bb'}^K \quad (42)$$

$$\hat{C}^{\kappa\kappa} \equiv C^{\kappa\kappa} + \frac{\sigma_e^2}{2\bar{n}_{\text{gal}}}. \quad (43)$$

where \bar{n}_{gal} is the mean number density of source galaxies used for the stacked lensing analysis and σ_e is the rms intrinsic ellipticity for the sum of two ellipticity components. For our fiducial Subaru HSC-type survey, $\bar{n}_{\text{gal}} \simeq 5 \text{ arcmin}^{-2}$ for source galaxies at $z_s > 1.5$, and we assume $\sigma_e = 0.35$, corresponding to ~ 0.25 for the rms per component. The Kronecker delta functions δ_{ij}^K and $\delta_{bb'}^K$ in Eqs. (41) and (42) enforce that the shot noise does not contaminate the cluster power spectra between clusters in different redshift bins and mass bins. Note that

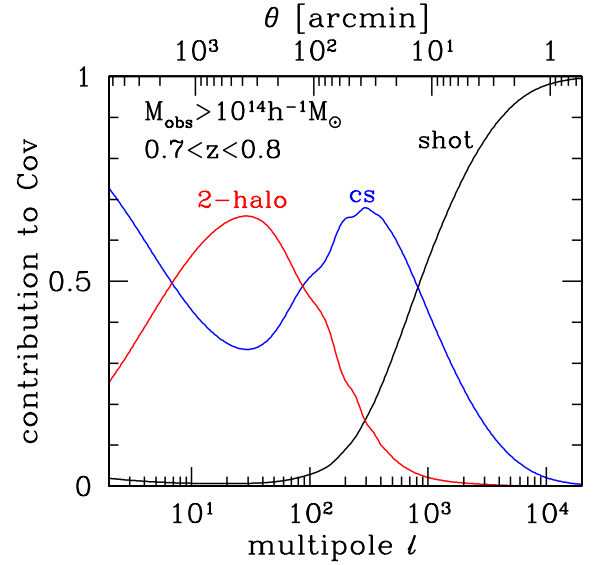


FIG. 8: Relative contributions to the diagonal covariance matrix elements of the stacked lensing signals as a function of multipole ℓ , for clusters with $M_{\text{obs}} > 10^{14} h^{-1} M_{\odot}$ and $0.7 < z < 0.8$. From right to left curves, we show the fractional contributions from the shot noise (“shot”), the cosmic shear (“cs”), and the sampling variance (“2-halo”) terms. See text for more details.

the shear-cluster power spectrum is not contaminated by shot noise.

Eq. (41) implies that the covariance of shear-cluster power spectrum consists of several contributions: (1) the shot noise term, which is proportional to $\sigma_e^2 / (\bar{n}_{i(b)} \bar{n}_{\text{gal}})$ and becomes important at high multipoles; (2) the cosmic shear contribution given as $(1/\bar{n}_{i(b)}) C^{\kappa\kappa}$; (3) the sampling variance (2-halo) contribution given by $C_{i(bb')}^{\text{hh}} \hat{C}^{\kappa\kappa} \delta_{ij}^K + C_{i(b)}^{\text{h}\kappa} C_{j(b')}^{\text{h}\kappa}$. Note that the contributions (1) and (2) are non-vanishing only if $i = j$ (the same redshift bins). In Fig. 8, we examine how each terms above contribute to the diagonal elements of covariance matrix (41) as a function of multipoles. As expected, the shot noise dominates at very small angles or very high multipoles, while the contribution from the cosmic shear is important over a range of angular scales from a few arcminutes to a degree scale (see also [68, 76, 77] for the cosmic shear contribution to cluster shear signals). Importantly for our method, the angular scales from a few to 10 arcminutes roughly correspond to the virial radii of massive clusters, and the shear signals around the virial radii are very sensitive to the halo mass, but rather insensitive to halo profile parameters such as the halo concentration and the halo off-centering parameter which are more sensitive to the shape of the shear profile (e.g., see [20] for such a discussion based on the actual weak lensing measurements). Hence the figure implies that the accuracy of halo mass estimation from the stacked lensing measurement is mainly limited by the cosmic shear contam-

ination. The sampling variance (3) gives significant contributions only at very large scales, $\ell \lesssim 10^2$ ($\theta \gtrsim 100'$), which suggests that this term can safely be neglected in the shear analysis of individual clusters for which tangential shear signals can be detected out to the virial radii at most. At the very large scales the cosmic shear term dominates again; this can be understood from the asymptotic behaviors of these terms, $(1/\bar{n}_{i(b)})C^{\kappa\kappa} \propto \ell^{n_s}$ for the cosmic shear and $(C^{\text{hh}})^2 \propto (C^{\text{hh}}C^{\kappa\kappa}) \propto (\ell^{n_s})^2$ for the sampling variance term in the limit of $\ell \rightarrow 0$, where $n_s \approx 1$ is the power spectrum tilt.

Similarly, the covariance matrix of cluster power spectrum and the cross-covariance matrix of C^{hh} and $C^{\text{h}\kappa}$ are

$$\text{Cov}(C_{i(bb')}^{\text{hh}}, C_{j(bb')}^{\text{hh}}) = \frac{4\pi}{\Omega_s} \frac{\delta_{\ell\ell'}^K}{(2\ell+1)\Delta\ell} \delta_{ij}^K \times \left[\hat{C}_{i(bb')}^{\text{hh}} \hat{C}_{j(bb')}^{\text{hh}} + \hat{C}_{i(bb')}^{\text{hh}} \hat{C}_{j(bb')}^{\text{hh}} \right], \quad (44)$$

and

$$\text{Cov}(C_{i(b)}^{\text{h}\kappa}, C_{j(b')}^{\text{hh}}) = \frac{4\pi}{\Omega_s} \frac{\delta_{\ell\ell'}^K}{(2\ell+1)\Delta\ell} \delta_{ij}^K \times \left[\hat{C}_{i(b)}^{\text{h}\kappa} C_{j(b')}^{\text{hh}} + \hat{C}_{i(b)}^{\text{h}\kappa} C_{j(b')}^{\text{hh}} \right]. \quad (45)$$

The Fisher matrices of the power spectrum observables are given as

$$F_{\alpha\beta}^{\text{PS}} = \sum_{\ell} \sum_{I,J} \frac{\partial \mathbf{D}_I(\ell)}{\partial p_{\alpha}} [\text{Cov}(\mathbf{D}(\ell), \mathbf{D}(\ell))]_{IJ}^{-1} \frac{\partial \mathbf{D}_J(\ell)}{\partial p_{\beta}}, \quad (46)$$

where the indices I, J run over the redshift and mass bins i, b and so on. At each multipole, if N_z redshift slices, N_M halo mass bins in each redshift slice, and N_{ℓ} multipole bins are taken, the dimension of $C_{i(bb')}^{\text{hh}}$ is $N_z \times N_{\ell} \times N_M(N_M+1)/2$, and that of $C_{i(b)}^{\text{h}\kappa}$ is $N_z \times N_{\ell} \times N_M$. The dimensions of the covariance matrix of each power spectrum and the cross-covariance are given by their squared or the product at each multipole. Under the Gaussian error assumption, there is no cross-covariance between different multipoles, and hence the summation in Eq. (46) is done at each multipole.

In computing the Fisher matrix $F_{\alpha\beta}^{\text{PS}}$, we include the power spectrum information up to the maximum multipole to $\ell_{\text{max}} = 10^4$, which roughly corresponds to $\theta_{\text{min}} \sim 1'$. While the choice may be conservative in the sense that significant signals can be detected at $\ell > 10^4$ (see Fig. 7), the stacked lensing signals near the cluster center are affected by various systematic effects ignored in this paper, such as the non-linearity of shear signals, the contributions from central galaxies, or more generally the effects due to baryonic physics. Our choice of $\ell_{\text{max}} = 10^4$ is therefore intended to minimize the impact of these systematic effects. Note that we properly include various nuisance parameters to model variations in the stacked lensing signals that can be quite important at $\ell_{\text{max}} < 10^4$, including the halo concentration parameters

and the halo off-set parameters. By marginalizing the parameter forecasts over these nuisance parameters, we have checked that the accuracies of cosmological parameters are not sensitive to the modes around the maximum multipoles, also because the modes at multipoles $\ell \gtrsim 10^3$ are limited by the shot noise contamination as explicitly shown below. We have also checked that the results are not largely changed if including up to an even higher maximum multipole such as $\ell_{\text{max}} = 2 \times 10^4$ or 3×10^4 .

On the other hand, the maximum angular scale we can observe should be related with the survey area Ω_s . Thus we estimate the minimum multipole ℓ_{min} using the relation $\ell_{\text{min}} \simeq \pi/\sqrt{\Omega_s/\pi}$. We use $\ell_{\text{min}} = 8$ for our fiducial survey area of 2000 deg^2 .

The shear-cluster and cluster-cluster power spectra have fairly smooth features in multipole space. Hence, we used the binned power spectra in multipole space to perform the summation in Eq. (46) over multipoles. We have checked that a finer binning of multipoles does not change the following results.

For reference, the covariance matrix of the stacked lensing profile in real space can also be computed as in [78] (also see [74] for the similar expression on the covariance of cosmic shear correlation functions):

$$\text{Cov}[\langle \gamma_+ \rangle_{i(b)}(\theta_m), \langle \gamma_+ \rangle_{j(b')}(\theta_n)] = \frac{1}{\Omega_s} \int \frac{\ell d\ell}{2\pi} \times \hat{J}_2(\ell\theta_m) \hat{J}_2(\ell\theta_n) \left[\hat{C}_{i(bb')}^{\text{hh}}(\ell) \hat{C}_{j(bb')}^{\kappa\kappa}(\ell) \delta_{ij}^K + C_{i(b)}^{\text{h}\kappa}(\ell) C_{j(b')}^{\text{h}\kappa}(\ell) \right]. \quad (47)$$

Here we consider the covariance between angles averaged within an annulus between $\theta_{k,\text{min}}$ and $\theta_{k,\text{max}}$ and so on. The Bessel function averaged over such a bin is defined by

$$\hat{J}_2(\ell\theta_m) = \frac{2}{\theta_{m,\text{max}}^2 - \theta_{m,\text{min}}^2} \int_{\theta_{m,\text{min}}}^{\theta_{m,\text{max}}} \theta d\theta J_2(\ell\theta). \quad (48)$$

At small scale ($\theta \ll 1$) the covariance matrix should be dominated by the shot noise. In this limit the covariance matrix can be simplified as

$$\text{Cov} \simeq \frac{\sigma_e^2}{2\pi(\theta_{m,\text{max}}^2 - \theta_{m,\text{min}}^2) \Omega_s \bar{n}_{\text{gal}} \bar{n}_{i(b)}} \delta_{mn}^K \delta_{ij}^K \delta_{bb'}^K. \quad (49)$$

Eq. (47) shows that, even for the Gaussian error case, the stacked shear profile of different angles are correlated with each other in contrast with the power spectrum covariance. The correlations are indeed significant for neighboring bins (e.g., see [79]). Thus to correctly extract cosmological information from the real-space stacked shear profile, we need to properly include the covariances between the measured shear profiles of different angles, which is not straightforward compared to the Fourier-space based analysis [79].

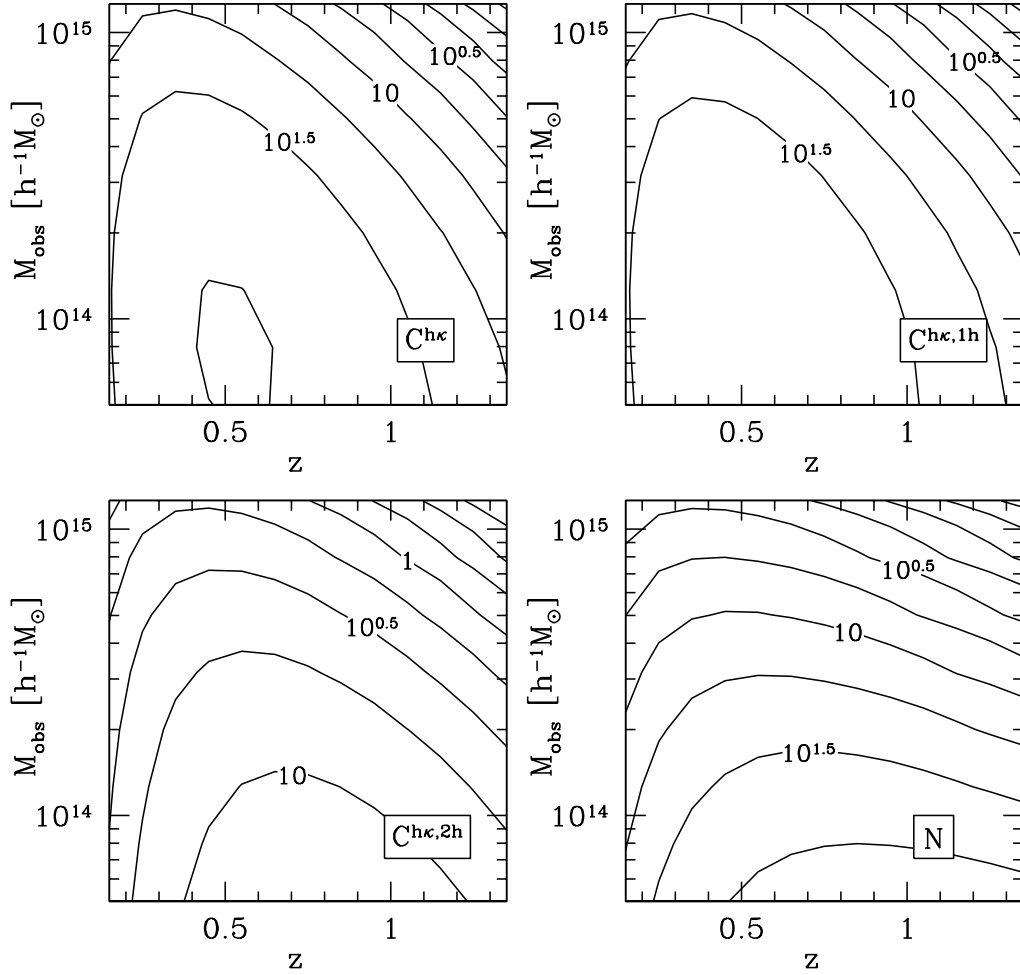


FIG. 9: The total signal-to-noise ratios for the stacked lensing signals as well as number counts of clusters, assuming the survey area of 2000 deg^2 and the bin sizes of $\Delta z = 0.1$ and $\Delta(\log M_{\text{obs}}) = 0.2$. The contours are spaced by $0.25 \text{ dex } S/N$. We show the signal-to-noise ratios for the total stacked lensing signal $C^{\text{h}\kappa}$ (Eq. [50]) (*upper-left panel*) and the contributions to it from 1-halo (*upper-right*) and 2-halo (*lower-left*) terms. The signal-to-noise ratios for the cluster number counts are also shown for reference (*lower-right*). Note that the signal-to-noise ratios scale with the survey area Ω_s (roughly) as $\propto \sqrt{\Omega_s}$.

2. Signal-to-Noise Ratios of Stacked Lensing

Using the power spectrum covariance we derived above, we here study the *total* signal-to-noise (S/N) ratio of the stacked shear measurement, integrated over angular scales considered, as a function of cluster redshifts and masses. The total S/N gives an indicator on the power of a given observable, measured from survey of interest, for constraining cosmological parameters (e.g., [74]). The total S/N for measuring the stacked lensing signals of clusters in the i -th redshift bin and the b -th mass bin can be simply expressed in Fourier space as

$$\left(\frac{S}{N}\right)^2 = \sum_{\ell} C_{i(b)}^{\text{h}\kappa}(\ell) [\text{Cov}(C^{\text{h}\kappa}, C^{\text{h}\kappa})]^{-1} C_{i(b)}^{\text{h}\kappa}(\ell). \quad (50)$$

Note that the total S/N in real space is similarly defined by using the covariance matrix (47), which has the same

amplitudes as the S/N above, because the power spectrum and the stacked lensing profile contain the equivalent information content at two point level.

Fig. 9 shows contours of the expected S/N for a Subaru HSC-type survey of 2000 deg^2 area coverage, as a function of cluster masses and redshifts, assuming their bin widths of $\Delta z = 0.1$ and $\Delta(\log M_{\text{obs}}) = 0.2$, respectively. Again notice that we assume the single population of source galaxies in this plot, source galaxies located at $z_s > 1.5$. The figure shows that the stacked lensing signals are detected at high significance ($S/N \gtrsim 10$) over a wide range of cluster masses and redshifts. Most of the signal-to-noise ratio comes mainly from the small-angle lensing signals, where the 1-halo term (Eq. [27]) is dominated. The 2-halo term or equivalently the large-angle signals can also be detected at marginal significance ($S/N \gtrsim 1$) in most mass and redshift bins. For comparison, we also show the signal-to-noise ratio for the num-

ber counts, which is similarly defined using Eqs. (13) and (37). The figure shows that a wide-field survey allows a significant detection of the number counts of clusters over a wide range of masses and redshifts.

The S/N estimate above allows us to argue how well we can measure the mean mass of clusters in each bin from the stacked lensing signals, which is the key in achieving the self-calibration of cluster mass-observable relation as described in Sec. II. The halo mass is sensitive to the overall amplitude of the stacked shear profile, with the shear amplitude at angular scales around the project virial radius roughly scaling with the halo mass as $\gamma_+ \propto M$ (e.g., [20]). Hence the mass calibration accuracy is roughly estimated as

$$\frac{\Delta M}{M} \sim \left(\frac{S}{N}\right)^{-1} \left(\frac{d \ln \gamma_+}{d \ln M}\right)^{-1}. \quad (51)$$

Fig. 9 implies that the mean mass of clusters can be measured to a few percent accuracy for halos with masses of a few $10^{14} h^{-1} M_\odot$ and over redshifts $0.3 \lesssim z \lesssim 1$. Since the shear signals also depend on other parameters such as cosmological parameters, the concentration parameters and the off-centering parameters, the genuine power of the mean halo mass estimation has to be realized taking into account marginalization over other parameters, as will be carefully studied below.

C. Fisher Matrix: Combining the Cluster Experiment and Stacked Lensing

In summary, the Fisher matrix for the joint experiment combining the cluster experiment (the number counts and the cluster-cluster power spectrum) and the stacked lensing information (the shear-cluster power spectrum) can be given as

$$F_{\alpha\beta}^{\text{CC+WL}} = F_{\alpha\beta}^{\text{N}} + F_{\alpha\beta}^{\text{PS}}, \quad (52)$$

where \mathbf{F}^{N} and \mathbf{F}^{WL} are given by Eqs. (39) and (46), respectively. In Eq. (52) we assumed that the number counts and the power spectrum observables are uncorrelated, where the former and the latter probe one-point and two-point correlation information on the underlying mass distribution. As carefully studied in [59], the cross-covariance between the number counts and the power spectra arises from the three-point correlation of the mass distribution, and an inclusion of the cross-covariance does not largely degrade the accuracies of cosmological parameter estimation as long as a sufficiently large number of model parameters are included. Hence, our approach above is a good approximation as the first step, although a more careful study including the full covariance contribution will be needed.

V. RESULTS

A. Parameters, Fiducial Model and Priors

1. Fiducial Model and Nuisance Parameters

We now estimate accuracies of the cosmological parameter estimation given the measurement accuracies of the observables, using the Fisher matrix formalism. This formalism assesses how well given observables can constrain cosmological parameters around a fiducial cosmological model. The parameter forecasts we obtain depend on the fiducial model and are also sensitive to the choice of free parameters.

We include all the key parameters that may affect the observables within the cold dark matter and dark energy cosmological framework. As for our fiducial cosmological model, which is based on the WMAP seven-year results [54], we include the following 9 cosmological parameters: the density parameters of matter, baryon and dark energy are $\Omega_M h^2 (= 0.134)$, $\Omega_b h^2 (= 0.0226)$, and $\Omega_{\text{DE}} (= 0.734)$ (note that we assume a flat universe); dark energy equation of state parameters are $w_0 (= -1)$ and $w_a (= 0)$; the primordial power spectrum parameters are the spectrum tilt $n_s (= 0.963)$, the running spectral index $\alpha_s (= 0)$, and the normalization parameter of primordial curvature perturbation, $\delta_\zeta (= 4.89 \times 10^{-5})$, where the values in the parentheses denote the fiducial parameter values. As an extension of dark energy cosmological model we also include the primordial non-Gaussianity which is modeled by the local-type parameter $f_{\text{NL}} (= 0)$. To be more specific we adopt the model [8, 57] in computing the halo mass function and the halo bias.

In addition, we include a number of nuisance parameters to model systematic errors involved in the observables. For the mass-observable relation, which is parametrized by $\ln M_{\text{bias}}$ and $\sigma_{\ln M}$, we allow more complicated dependences on redshift and halo mass by adopting the following form:

$$\ln M_{\text{bias}}(M, z) = \ln M_{\text{b},0} + \sum_{i=1}^3 q_{\text{b},i} [\ln(M/M_{\text{piv}})]^i + \sum_{i=1}^3 s_{\text{b},i} z^i, \quad (53)$$

$$\sigma_{\ln M}(M, z) = \sigma_{\ln M,0} + \sum_{i=1}^3 q_{\sigma_{\ln M},i} [\ln(M/M_{\text{piv}})]^i + \sum_{i=1}^3 s_{\sigma_{\ln M},i} z^i, \quad (54)$$

where we choose $M_{\text{piv}} = 3 \times 10^{14} h^{-1} M_\odot$, and $\ln M_{\text{b},0}$, q_i , s_i , \dots are free parameters. The form above has been adopted by previous work (e.g., [11]). The fiducial values for these parameters are $\sigma_{\ln M,0} = 0.3$, and the other parameters such as $\ln M_{\text{b},0}$, $q_{\text{b},i}$ and $s_{\text{b},i}$ are set to zero.

The source redshift uncertainty affecting the stacked lensing signals is parametrized by the mean redshift parameter $z_m (= 1)$ in the source redshift distribution (see Eq. [17]). The systematic errors in the small-scale

Cosmological paras.	$\Omega_{\text{DE}}, \Omega_M h^2, \Omega_b h^2, n_s, \alpha_s, w_0, w_a, \delta_\zeta, f_{\text{NL}}$	
Source redshift	$z_m (\equiv 3z_0)$	Eq. (17)
Concentration parameter: $C(M, z)$	$A_{\text{vir}}, B_{\text{vir}}, C_{\text{vir}}$	Eq. (26)
Halo off-centering paras: f_{cen}, σ_s	$f_{\text{cen}}(M, z) = f_{\text{cen},0} + p_{\text{cen},M} \ln(M/M_{\text{piv}}) + p_{\text{cen},z} \ln(1+z)$ $\sigma_s(M, z) = \sigma_{s,0} + p_{\sigma_s,M} \ln(M/M_{\text{piv}}) + p_{\sigma_s,z} \ln(1+z)$	Eq. (34)
Mass-obs. relation: $\ln M_{\text{bias}}, \sigma_{\ln M}$	$\ln M_{\text{bias}} = \ln M_{b,0} + \sum_{i=1}^3 q_{b,i} [\ln(M/M_{\text{piv}})]^i + \sum_{i=1}^3 s_{b,i} z^i$ $\sigma_{\ln M} = \sigma_{\ln M,0} + \sum_{i=1}^3 q_{\sigma_{\ln M},i} [\ln(M/M_{\text{piv}})]^i + \sum_{i=1}^3 s_{\sigma_{\ln M},i} z^i$	Eq. (9)

TABLE I: Parameters included in our Fisher matrix analysis. We include 9 cosmological parameters as well as 24 nuisance parameters to quantify the impact of possible residual systematic errors on the cosmological parameter estimation. In total we include 33 parameters. The fiducial values of each parameters are given in the text.

stacked shear profile are the halo concentration parameter parametrized by three parameters, $A_{\text{vir}}, B_{\text{vir}}$ and C_{vir} (see Eq. [26] below for their fiducial values), and the halo off-centering effect given by the two parameters f_{cen} and σ_s (Eq. [34]). Similarly, to include possible mass and redshift dependences for the offset parameters, which are poorly known theoretically, we employ a simple form given by

$$f_{\text{cen}}(M, z) = f_{\text{cen},0} + p_{\text{cen},M} \ln(M/M_{\text{piv}}) + p_{\text{cen},z} \ln(1+z), \quad (55)$$

$$\sigma_s(M, z) = \sigma_{s,0} + p_{\sigma_s,M} \ln(M/M_{\text{piv}}) + p_{\sigma_s,z} \ln(1+z). \quad (56)$$

Note that the nuisance parameters for σ_s are in units of $h^{-1}\text{Mpc}$. The fiducial values are $f_{\text{cen}} = 0.75 + 0.05 \ln(M/M_{\text{piv}})$, i.e., $f_{\text{cen},0} = 0.75$, $p_{\text{cen},M} = 0.05$ and $p_{\text{cen},z} = 0$; $\sigma_{s,0} = 0.42 h^{-1}\text{Mpc}/D_A(z)$, $p_{\sigma_s,M} = 0$ and $p_{\sigma_s,z} = 0$.

Thus we include 33 parameters in the Fisher matrix analysis; 9 cosmological parameters and 24 nuisance parameters (see Table I for a brief summary). Unless otherwise specified, we do not add any prior on the nuisance parameters.

We also need to specify survey parameters. Thus far we have employed the survey parameters that resemble the planned Subaru HSC survey (see Eq. [17]). For a broader application of the method proposed in this paper we also consider other survey parameters which roughly resemble other imaging surveys being planned, DES and LSST. Table II summarizes the assumed survey parameters. We adopt the method in [74] (see around Eq. [20] of the paper) to estimate the mean redshift and the available number density of galaxies for each survey.

For all surveys, we employ the same halo mass threshold $M_{\text{obs}} > 10^{14} h^{-1} M_\odot$, which makes it easier to compare the results between different surveys. We consider 5 mass bins for each redshift slice, with the bin width of $\Delta(\log M_{\text{obs}}) = 0.2$ (for the highest mass bin, we extend the upper limit of the mass to infinity). The maximum cluster redshift is set to $z_{\text{max}} = 1.4$, which is approximately the maximum cluster redshift detectable via optical imaging surveys including y -band data, except for DES for which we adopt $z_{\text{max}} = 1$ given the shallower

depth. The cluster redshift bin width is $\Delta z = 0.1$ for all the surveys. For the source galaxy population needed for the stacked lensing we use galaxies at $z_s > 1.5$ for HSC and LSST, and at $z_s > 1.1$ for DES, respectively. Assuming the depth of each survey we can compute the available number density of source galaxies, which is needed to quantify the intrinsic ellipticity noise. We simply assume $\sigma_e = 0.35$ for the rms intrinsic ellipticities (sum of two components) for all the surveys.

2. Priors

As stated above, unless explicitly expressed, we do not use any priors on the 24 nuisance parameters. Therefore, we can address how combining the cluster experiments and the stacked lensing allows to self-calibrate these nuisance parameters.

However, using probes of large-scale structure alone is not powerful enough to constrain all the cosmological parameters simultaneously. Rather, combining the large-scale structure probes with constraints from Cosmic Microwave Background (CMB) temperature and polarization anisotropies significantly helps to lift parameter degeneracies. In this paper we use the CMB priors expected from the Planck satellite mission. When computing the Fisher matrix for the CMB we employ 9 parameters in total, 8 from our fiducial cosmological parameter set (we do not include any constraints on f_{NL} from CMB in order to examine the pure power of clusters and weak lensing in constraining f_{NL}) plus the Thomson scattering depth to the last scattering surface ($\tau = 0.089$). We used the publicly-available CAMB code [80], based on the CMBFAST [81], to compute the angular power spectra of temperature anisotropy, E -mode polarization and their cross-correlation. Note that we ignored B -mode spectra arising from the primordial gravitational wave. The details of our CMB Fisher matrix calculation can be found from [59]. The Fisher matrix for the joint experiments combining the CMB information with the method studied in this paper is simply given by adding the CMB Fisher matrix to the matrix in Eq. (52), i.e., $\mathbf{F} = \mathbf{F}^{\text{CMB}} + \mathbf{F}^{\text{N}} + \mathbf{F}^{\text{PS}}$. The Thomson scattering depth τ is marginalized over before the CMB Fisher matrix is

Survey	Ω_s [deg ²]	z_m	$\bar{n}_{\text{gal,tot}}$ [arcmin ⁻²]	\bar{n}_{gal} [arcmin ⁻²]	$z_{s,\text{min}}$	$M_{\text{obs-range}}$ [$h^{-1}M_{\odot}$]	N_M	$z\text{-range}$	N_z	$\ell\text{-range}$
HSC (2000deg ²)	2000	1.0	30	5.2	1.5	$10^{14} < M_{\text{obs}}$	5	$0.1 < z < 1.4$	13	$8 < \ell < 10^4$
HSC (1500deg ²)	1500	1.0	30	5.2	1.5	$10^{14} < M_{\text{obs}}$	5	$0.1 < z < 1.4$	13	$8 < \ell < 10^4$
DES	5000	0.7	10	1.5	1.1	$10^{14} < M_{\text{obs}}$	5	$0.1 < z < 1.0$	9	$5 < \ell < 10^4$
LSST	20000	1.2	50	14	1.5	$10^{14} < M_{\text{obs}}$	5	$0.1 < z < 1.4$	13	$2 < \ell < 10^4$

TABLE II: The summary of survey parameters adopted in this paper. The parameters N_M and N_z denote the numbers of cluster mass and redshift bins, respectively. Note that the survey parameter set of HSC (2000deg²) is same as the fiducial parameter set used in previous sections. The parameters $\bar{n}_{\text{gal,tot}}$ and \bar{n}_{gal} denote the number densities of source galaxies at all redshifts and at redshift $z_s > z_{s,\text{min}}$, respectively, where the latter is used for the weak lensing analysis in this paper.

Method	$\sigma(\Omega_{\text{DE}})$	$\sigma(w_0)$	$\sigma(w_a)$	FoM	z_{piv}	$\sigma(f_{\text{NL}})$	$\sigma(\ln \Omega_M h^2)$	$\sigma(\ln \Omega_b h^2)$	$\sigma(n_s)$	$\sigma(\alpha_s)$	$\sigma(\ln \delta_{\zeta})$
Planck	—	—	—	—	—	—	0.0102	0.0086	0.0226	0.0068	0.0174
+ \mathbf{N}	0.099	0.62	2.17	1.4	0.32	—	0.0101	0.0085	0.0218	0.0066	0.0169
+ $\mathbf{N} + \mathbf{C}^{\text{hh}}$	0.035	0.37	1.13	7.5	0.46	15.6	0.0098	0.0079	0.0201	0.0061	0.0158
+ $\mathbf{C}^{\text{h}\kappa}$	0.056	0.44	1.12	5.1	0.56	86.9	0.0099	0.0080	0.0205	0.0063	0.0161
+ $\mathbf{N} + \mathbf{C}^{\text{hh}} + \mathbf{C}^{\text{h}\kappa}$	0.023	0.22	0.60	28.6	0.56	14.5	0.0059	0.0068	0.0189	0.0058	0.0143
+ $\mathbf{N} + \mathbf{C}^{\text{hh}} + \mathbf{C}^{\text{h}\kappa} + \mathbf{C}^{\kappa\kappa}$	0.022	0.22	0.59	32.4	0.57	14.3	0.0053	0.0065	0.0124	0.0038	0.0104
+ $\mathbf{N} + \mathbf{C}^{\text{hh}} + \mathbf{C}^{\text{h}\kappa} + \text{BAO}$	0.017	0.18	0.48	52.7	0.58	14.2	0.0041	0.0066	0.0188	0.0058	0.0141
+ $\mathbf{N} + \mathbf{C}^{\text{hh}} + \mathbf{C}^{\text{h}\kappa} + \mathbf{C}^{\kappa\kappa} + \text{BAO}$	0.017	0.18	0.47	54.8	0.58	14.0	0.0040	0.0063	0.0123	0.0038	0.0103

TABLE III: Expected marginalized errors (68% C.L.) on each cosmological parameter for different combinations of cosmological probes: the column labeled as “Planck” shows the errors expected from the CMB information alone; the following columns are the results expected by further adding the cluster number counts (\mathbf{N}), the cluster-cluster power spectra (\mathbf{C}^{hh}), the shear-cluster spectra ($\mathbf{C}^{\text{h}\kappa}$), the cosmic shear spectra ($\mathbf{C}^{\kappa\kappa}$), and the geometrical constraints expected from the BOSS BAO information (see text for details). The errors include marginalization over other parameters including nuisance parameters (see Tab. I). However note that we did not employ any priors on the nuisance parameters. The columns labeled as “FoM” and “ z_{piv} ” denote the dark energy figure of merit and the pivot redshift, respectively (see text for details). We assume the survey parameters for HSC (2000 deg²) in Tab. II, for the cluster counts and the power spectrum measurements (\mathbf{C}^{hh} , $\mathbf{C}^{\text{h}\kappa}$). Note that z_{piv} denotes the pivot redshift at which the dark energy equation of state is best constrained. The element labeled as “—” denotes that the parameter is not well constrained by the observables.

added to other constraints.

By the time when the imaging surveys above come online, stringent cosmological constraints will be available from the ongoing Baryon Oscillation Spectroscopic Survey (BOSS) [99], which gives a geometrical probe of cosmological distances via the baryon acoustic oscillation (BAO) experiment [82]. Using the method in [83], we compute the Fisher matrix expected from the BOSS experiment. To be more precise, we will add, to the Fisher matrix, the expected geometrical information on the Hubble expansion rates and the angular diameter distances to the redshifts, $z \simeq 0.65$, which are relevant for $\Omega_M h^2$, Ω_{DE} , w_0 , w_a in our parameters.

Finally we will also study how the cosmological constraints can be improved by adding another power spectrum available from the same imaging survey data, the cosmic shear power spectrum $C^{\kappa\kappa}$ for the same source galaxies. Since the cluster-cluster, shear-cluster and cosmic shear power spectra at large angles depend on the halo bias b_h in different ways, roughly $C^{\text{hh}} \propto b_h^2 P_m$, $C^{\text{h}\kappa} \propto b_h P_m$ and $C^{\kappa\kappa} \propto P_m$, combining all the spectra may help to break the degeneracies between the halo bias and other parameters further. However, note that the

self-calibration of nuisance parameters can be achieved only if focusing on the single source galaxy population for lensing. Thus, we include the cosmic shear power spectrum without tomography. For the cosmic shear $C^{\kappa\kappa}$, we include the spectrum only up to $\ell_{\text{max}} = 10^3$ as the cosmic shear at small scales is subject to various uncertainties. We take proper account of the cross-covariance of $C^{\kappa\kappa}$ with $C^{\text{h}\kappa}$ and C^{hh} when adding constraints from $C^{\kappa\kappa}$.

B. Parameter Forecasts

Table III summarizes the 68% error on each cosmological parameter, marginalized over other parameter uncertainties including nuisance parameters in Table I. Here we have assumed survey parameters for the HSC survey of 2000 deg² coverage given in Table II. The first row shows the constraints expected from the Planck data alone, while the other rows show the constraints by further adding the large-scale structure probes. It is shown that the parameter constraints can be continuously improved by adding the different observables, the cluster counts, the cluster-cluster power spectrum, the

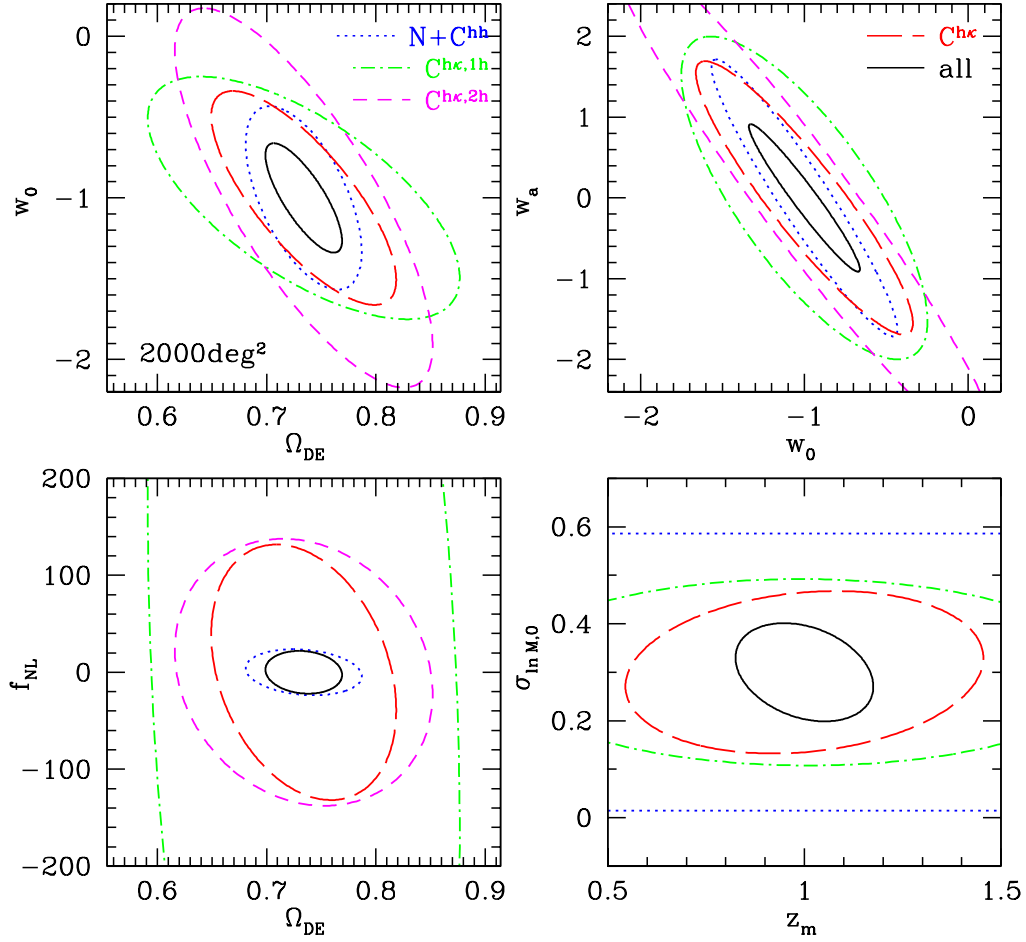


FIG. 10: Projected 68% confidence limit ($\Delta\chi^2 = 2.3$) constraints in various parameter spaces; $\Omega_{\text{DE}}-w_0$ plane (*upper-left panel*), w_0-w_a plane (*upper-right*), $\Omega_{\text{DE}}-f_{\text{NL}}$ plane (*lower-left*), and $z_m-\sigma_{\ln M,0}$ plane (*lower-right*). The survey area is assumed to 2000 deg^2 . The different curves indicate constraints from different measurements; the number counts plus the cluster-cluster correlation function (*dotted*), the 1-halo (*dot-dashed*) and 2-halo (*short dashed*) terms of stacked lensing signals and their sum (*long dashed*), and the total constraints from the combination of all measurements (*solid*). The Planck prior is added in all cases.

stacked lensing, the cosmic shear power spectrum, and the BAO experiment. We should again stress that we did not add any priors on nuisance parameters in Table I, and therefore the parameter constraints are as a result of the self-calibration of those systematic effects attained by combining the different probes. The previous works [9, 11, 38–40] have studied the combination of cluster number counts and cluster-cluster correlation functions (so-called “self-calibrated cluster counts”), which is essentially represented by the column denoted by “ $+N + C^{\text{hh}}$ ”. We find that an additional calibration of cluster masses from the stacked weak lensing signals significantly improves constraints on each of the dark energy parameters, by a factor of 2 or so, even when various uncertainties associated with stacked lensing signals, such as the source redshift uncertainty, off-centering, and concentration parameters, are marginalized over. The resulting constraints on dark energy equation of state is in

fact quite comparable to the constraints expected from tomographic cosmic shear without any marginalization over systematic errors [74].

A useful parameter that quantifies the power of a given survey for constraining dark energy equation of state is so-called the Figure of Merit (FoM) defined by [1]

$$\text{FoM} = \frac{1}{\sigma(w_a)\sigma(w_p)} = \frac{1}{\sqrt{\det(\text{Cov}[w_0, w_a])}}, \quad (57)$$

where w_p is dark energy equation of state at the “pivot” redshift, at which the dark energy equation of state is best constrained [1]. The FoM is inversely proportional to the area of the error ellipse in the w_0-w_a plane. Thus, the larger the FoM is, constraints on dark energy models are tighter. Table III shows that adding the stacked lensing signals improves the FoM by a factor of ~ 4 compared with the cluster experiment alone (number counts plus the cluster-cluster power spectrum) in our fiducial

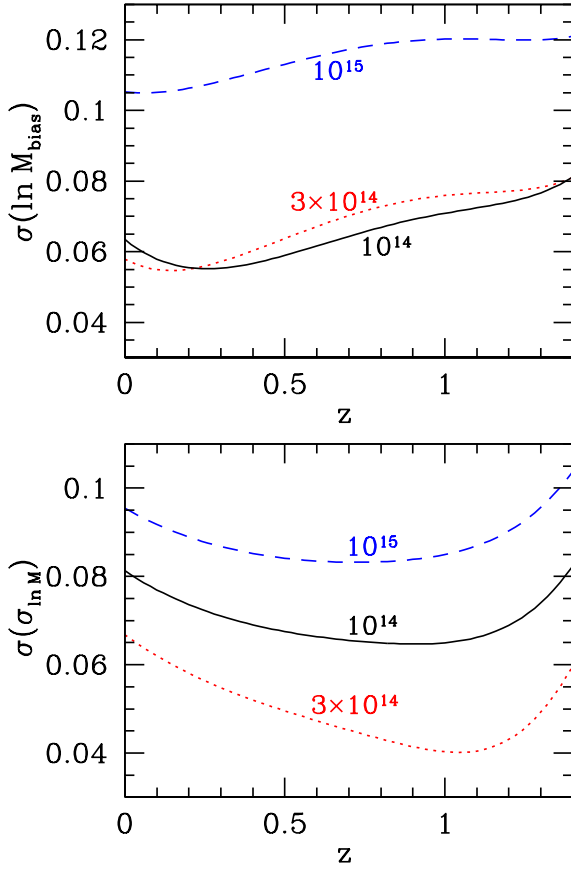


FIG. 11: Marginalized errors on $\ln M_{\text{bias}}$ (upper panel) and $\sigma(\ln M)$ (lower), the parameters in the mass-observable relation (see Eq. [9]), as a function of cluster redshifts, constrained from the combination of all the observables (except for the cosmic shear and BAO). The errors are shown for three different cluster masses, $M = 10^{14} h^{-1} M_{\odot}$ (solid curve), $3 \times 10^{14} h^{-1} M_{\odot}$ (dotted), and $10^{15} h^{-1} M_{\odot}$ (dashed).

setting. This result appears to be consistent with a recent similar analysis by [84], although no systematic error associated with the stacked lensing analysis has been considered in their Fisher matrix analysis.

It would be also informative to study how a different combination of the observables can break the parameter degeneracies. Fig. 10 shows projected 68% error ellipses in various two-parameter sub-spaces of the parameters. The dotted and long-dashed curves show the error ellipses expected from the cluster experiments (the number counts plus the cluster-cluster power spectrum) and the stacked lensing, respectively. For comparison the dot-dashed and short-dashed curves show the results from each of the small-angle (1-halo term) and large-angle (2-halo term) signals of the stacked lensing, respectively. The innermost solid curve is the ellipse by combining all the measurements (except for the BAO and the cosmic shear power spectrum), showing that the ellipse significantly shrinks compared to any of the ellipses of one particular observable. This improvement of parameter

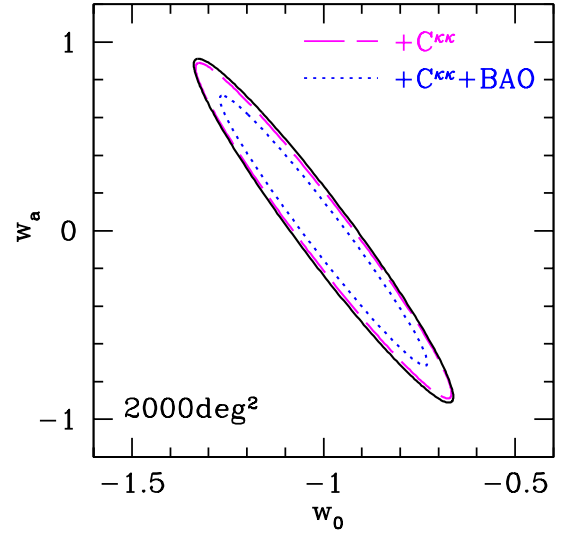


FIG. 12: The improvements of the marginalized constraints in the w_0 - w_a plane by adding the cosmic shear power spectrum ($C^{\kappa\kappa}$) for the same source galaxy population as that used in the stacked lensing analysis, and the BAO geometrical information expected from the SDSS-III BOSS survey.

constraints is due to the self-calibration of nuisance parameters, and the lower-right panels explicitly shows one example: the mean source redshift is directly estimated from the observables (self-calibrated), without any prior, to an accuracy of $\sigma(z_m) \sim 0.1$ or so. Finally our results indicate that primordial non-Gaussianity can be constrained to $\sigma(f_{\text{NL}}) \sim 15$, which is mainly from the cluster observables (see also [9, 11]).

To see how well cluster masses are calibrated by the combination of stacked weak lensing and the cluster experiments, in Fig 11 we show the marginalized 68% error on the parameters in the mass-observable relation, $\ln M_{\text{bias}}$ and $\sigma(\ln M)$, as a function of cluster masses and redshifts, based on Eqs. (53) and (54). We find that the halo mass bias $\ln M_{\text{bias}}$ is constrained to $\sigma(\ln M_{\text{bias}}) \sim 0.07$ for a wide range of cluster masses and redshifts, indicating that cluster masses are determined at $\sim 7\%$ accuracy, even the other parameters are marginalized over. The mass calibrations of more massive clusters are less uncertain, simply because of the smaller number of clusters available for the stacked lensing analysis (see also Fig. 9).

Fig. 12 shows how the dark energy constraints, w_0 and w_a , can be further improved by adding the cosmic shear power spectrum of the same source galaxy population ($z_s > 1.5$) and the BOSS BAO information. The figure shows that the BOSS BAO information is useful to improve the dark energy constraints. More quantitatively, the marginalized errors on w_0 and w_a are improved, from $\sigma(w_0) = 0.22$ and $\sigma(w_a) = 0.60$, to $\sigma(w_0) = 0.18$ and $\sigma(w_a) = 0.47$ by adding both the cosmic shear power spectrum and the BOSS BAO information. The FoM

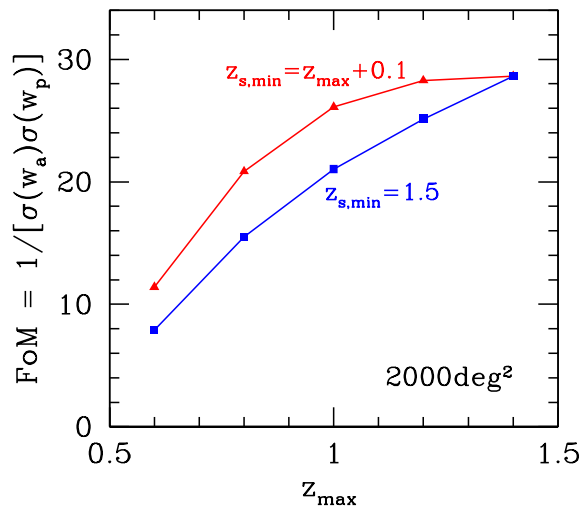


FIG. 13: The Figure of Merit (FoM) from the combination of the stacked lensing, the number counts, and the cluster-cluster correlation function, as a function of the maximum cluster redshift z_{\max} . The filled squares indicate the case that the minimum source redshift is fixed to $z_{s,\min} = 1.5$, whereas the case that the minimum source redshift is set to $z_{s,\min} = z_{\max} + 0.1$, is shown by the filled triangles.

value is improved by a factor of 1.9, from 28.6 to 54.8 (see also Table III). For comparison, the BOSS BAO information alone (with the Planck prior) has the FoM value of 19.2. Thus the BAO information appears to be highly complementary to the constraints from the imaging survey.

The stacked weak lensing has been thought to provide a powerful method to constrain the concentration-mass relation (e.g., [85]). However, in our Fisher matrix analysis, the marginalized errors on the concentration parameters, $\sigma(A_{\text{vir}}) = 3.9$, $\sigma(B_{\text{vir}}) = 0.09$, and $\sigma(C_{\text{vir}}) = 0.3$, are not so impressive. The reason is that these parameters are strongly degenerate with each other, and also with off-centering parameters (f_{cen} and σ_s). Our result therefore may suggest a critical difficulty in measuring the concentration-mass relation from the stacked weak lensing technique. Rather the information can be efficiently extracted by combining the weak and strong lensing information on individual cluster basis (e.g., [86–88]).

To understand the sensitivity of cluster redshifts to the dark energy constraints, we study how the dark energy constraints change with the maximum cluster redshift. Fig. 13 shows the FoM as a function of the maximum cluster redshift z_{\max} used for the analysis, for the same bin width of $\Delta z = 0.1$. We find that FoM changes rapidly with the maximum cluster redshifts particularly below 1, indicating the importance of deep cluster surveys to include clusters out to $z \gtrsim 1$. We do gain by adding clusters at $z > 1$ if we fix the minimum source redshift $z_{s,\min}$ to $z_{s,\min} = 1.5$. However, the improvement in the FoM at $z > 1$ becomes rather small if we set $z_{s,\min} = z_{\max} + 0.1$, because the additional information from high

redshift clusters can be to some extent compensated by the change of the number density of background source galaxies.

C. Effect of Priors

Thus far we adopted no prior on the nuisance parameters. However, in practice, we expect that there are external constraints on some of these parameters. For instance, photometric redshifts, which are required to define the source galaxy sample in the first place, naturally provide some prior information on z_m . The fraction and offset distributions of off-centering galaxies may be inferred from mock galaxy catalogs in N -body simulations [21] or directly from a detailed measurement of individual clusters [68]. For cluster observables we may be able to further refine the mass-observable relations by using detailed studies of individual clusters or combining different information from optical, lensing, X-ray and SZ measurements. Here we explore how such priors help to improve the parameter constraints.

The result is shown in Fig. 14. As specific examples, we add priors on the mean redshift of the source galaxy distribution, z_m , on the standard deviation of the cluster offsets, σ_s , on the halo mass bias of the cluster mass-observable relation, $\ln M_{\text{bias}}$, and on the mass scatter $\sigma_{\ln M}$. We find that the prior $\sigma(z_m) \lesssim 0.1$ indeed improves constraints on dark energy, although the improvement of the FoM is only up to about 10%. This again implies that the self-calibration of the source redshift is achieved by combining the different observables, well enough not to degrade our cosmological results. We, however, comment that a marginally accurate photo- z information is needed for selecting *source* galaxies for our stacked lensing analysis. An imperfect photo- z information causes a contamination from foreground or cluster member galaxies to the source galaxy population, which dilutes the stacked lensing signals. We will come back to this issue later. On the other hands, Fig. 14 indicates that priors on σ_s help improve the FoM. The result, in turn, confirms the previous claims that the off-centering is one of the biggest uncertainties inherent to the stacked weak lensing analysis [21].

The priors on the mass-observable relations have a greater impact on the FoM, because the dark energy constraints are mainly from cluster observables in the method studied in this paper. A few percent level prior on $\ln M_{\text{bias}}$ or $\sigma_{\ln M}$, if available, can improve the FoM by a factor of 2 and 1.3, respectively. The result suggests the importance of detailed studies of individual clusters for accurately calibrating the mass-observable relation, as has been done in [25, 89].

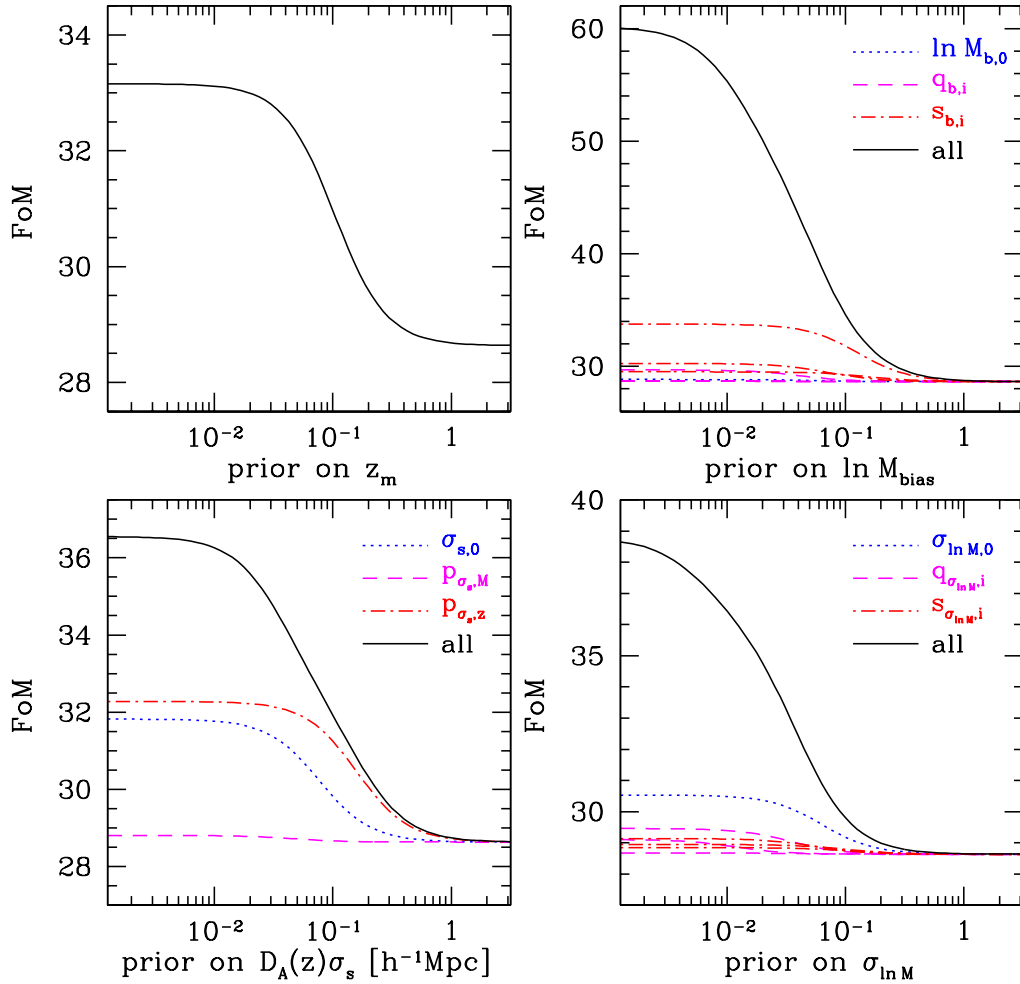


FIG. 14: The Figure of Merit (FoM) as a function of priors on various nuisance parameters to model the systematic errors: the mean source redshift z_m (*upper-left panel*), the cluster off-centering parameter σ_s (*lower-left*; in units of $h^{-1}\text{Mpc}$), the mass bias parameter of the cluster-mass observable relation $\ln M_{\text{bias}}$ (*upper-right*), and its mass scatter $\sigma_{\ln M}$ (*lower-right*). For the parameters σ_s , $\ln M_{\text{bias}}$ and $\sigma_{\ln M}$, we add the priors on parameters in Table I: the overall amplitude parameter, the halo mass dependence, the redshift dependence or all the parameters.

D. Predictions for Various Surveys

Next we tune survey parameters to several future wide-field optical imaging surveys, in which the stacked cluster lensing analysis studied in this paper is feasible, to study/compare their powers as a dark energy probe. Specifically, we consider the following surveys: HSC, DES and LSST.

The marginalized errors on dark energy parameters and f_{NL} are summarized in Table IV, and the projected error ellipses in the w_0 - w_a plane are presented in Fig. 15. The difference of FoM between HSC of 1500 and 2000 deg^2 , and LSST surveys can be understood by their differences in the survey area. The FoM roughly scales with the survey area as $\text{FoM} \propto \Omega_s$, and the difference between the FoM values of HSC and LSST can approximately be explained by this relation. On the other hand,

the FoM from DES is rather small despite its large area coverage of 5000 deg^2 . This is because DES is shallower than HSC and LSST, thereby yielding a narrower window of the redshift sensitivity to dark energy parameters due to the smaller number density of source galaxies and the lower maximum cluster redshift (see Table II). In all the surveys, the FoM is improved by a factor of 2 – 4 by adding the stacked weak lensing signals (see also Fig. 15), suggesting the powerful complementarity of stacked weak lensing to cluster cosmology. Table V summarize improvements of constraints in each survey by adding the cosmic shear measurement for the same source sample and the BOSS BAO information.

Survey	$N+C^{hh}$					$C^{h\kappa}$					$N+C^{hh}+C^{h\kappa}$				
	$\sigma(\Omega_{DE})$	$\sigma(w_0)$	$\sigma(w_a)$	FoM	$\sigma(f_{NL})$	$\sigma(\Omega_{DE})$	$\sigma(w_0)$	$\sigma(w_a)$	FoM	$\sigma(f_{NL})$	$\sigma(\Omega_{DE})$	$\sigma(w_0)$	$\sigma(w_a)$	FoM	$\sigma(f_{NL})$
HSC (2000deg ²)	0.035	0.37	1.13	7.5	15.6	0.056	0.44	1.12	5.1	86.9	0.023	0.22	0.60	28.6	14.5
HSC (1500deg ²)	0.040	0.42	1.26	6.0	18.0	0.062	0.48	1.24	4.1	99.9	0.026	0.26	0.69	21.9	16.8
DES	0.026	0.27	0.82	14.0	10.9	0.053	0.52	1.39	4.7	66.3	0.020	0.22	0.62	30.7	10.3
LSST	0.011	0.12	0.38	59.4	2.3	0.016	0.12	0.29	54.0	13.0	0.007	0.06	0.16	322.2	2.2

TABLE IV: Forecasts of cosmological parameters estimated from the Fisher matrix analysis. We compare three upcoming surveys, HSC, DES and LSST. All errors are 68% errors, after marginalizing over the other parameters, expected from the combination of the cluster number counts (N), the cluster power spectra (C^{hh}), and the stacked weak lensing signals ($C^{h\kappa}$). No prior is added on nuisance parameters. The Planck prior is added to all cases.

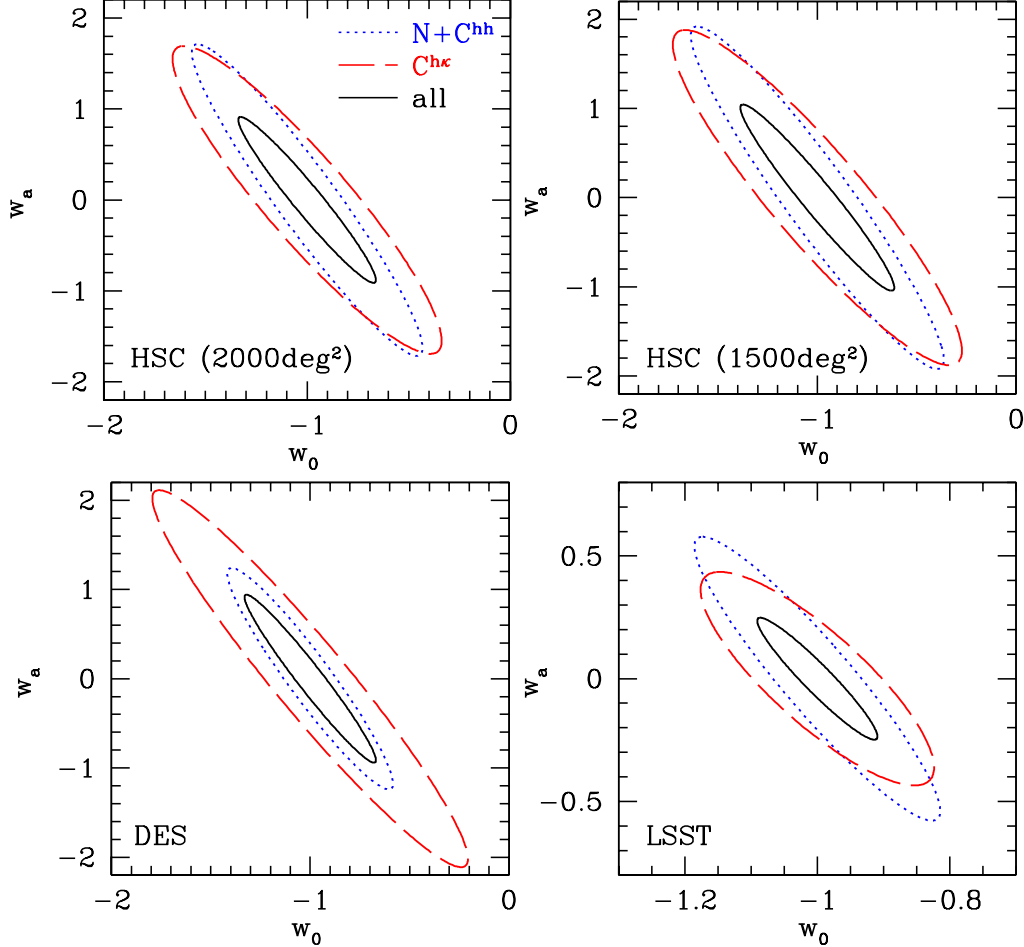


FIG. 15: Marginalized constraints in the w_0 - w_a plane for three different future surveys, HSC (*upper-left and upper-right panels*), DES (*lower-left*), and LSST (*lower-right*). The different curves are as in Fig. 10, i.e., the dotted curves denote constraints from the cluster number counts and the cluster-cluster correlation functions, the dashed curves are constraints from the stacked weak lensing (both 1- and 2-halo terms), and the solid curves show the combined constraints. While the Planck prior is added to all the ellipses, no prior is added to nuisance parameters.

VI. DISCUSSIONS ON OTHER SYSTEMATICS

While our analysis properly takes account of a number of key systematic effects, such as the mass-observable relation, the mean source redshift for weak lensing analysis, and the offset of cluster centers, there are still a number

of potential systematics that could affect our results. In this section, we briefly discuss these effects.

Perhaps one of the most important effects ignored in this paper is the error on cluster redshifts. In the future imaging surveys as considered above, cluster redshifts are thought to be measured using the photometric redshift

Survey	$+C^{\kappa\kappa}$					+BAO					$+C^{\kappa\kappa}$ +BAO				
	$\sigma(\Omega_{\text{DE}})$	$\sigma(w_0)$	$\sigma(w_a)$	FoM	$\sigma(f_{\text{NL}})$	$\sigma(\Omega_{\text{DE}})$	$\sigma(w_0)$	$\sigma(w_a)$	FoM	$\sigma(f_{\text{NL}})$	$\sigma(\Omega_{\text{DE}})$	$\sigma(w_0)$	$\sigma(w_a)$	FoM	$\sigma(f_{\text{NL}})$
HSC (2000deg ²)	0.022	0.22	0.59	32.4	14.3	0.017	0.18	0.48	52.7	14.2	0.017	0.18	0.47	54.8	14.0
HSC (1500deg ²)	0.025	0.25	0.67	24.8	16.5	0.018	0.20	0.52	45.0	16.3	0.018	0.19	0.51	46.7	16.1
DES	0.019	0.21	0.60	36.3	10.1	0.016	0.18	0.48	53.4	10.0	0.015	0.17	0.48	56.4	9.9
LSST	0.006	0.06	0.16	348.1	2.2	0.006	0.06	0.16	338.9	2.2	0.006	0.06	0.16	361.2	2.2

TABLE V: The improvements of cosmological constraints by adding extra constraints from the cosmic shear measurements ($C^{\kappa\kappa}$) using the same source galaxy sample as used in the stacked weak lensing analysis and from the baryon acoustic oscillation observations expected from the SDSS-III BOSS (BAO).

technique. [90] studied how the photo- z errors of clusters affect the cluster number counts, and then argued that photometric redshifts have to be accurate at $\lesssim 1\%$ level in order not to degrade dark energy constraints significantly. In fact this accuracy is almost reachable in future surveys, as we can use several tens of member galaxies to determine cluster redshifts accurately (e.g., [91]). We should comment that, if a redshift survey of Luminous Red Galaxies (LRGs) is available from the imaging survey region, such as the SDSS survey, the LRG catalog can be used to construct a secure catalog of clusters with spectroscopic redshifts. The LRGs are very likely to be one of the brightest cluster galaxies, and are relatively easy to measure their spectroscopic redshifts as they are bright. Thus the LRG catalog is enormously helpful in constructing a homogeneous catalog of clusters, by searching for member galaxies surrounding each LRG with deeper imaging survey. This is indeed the case for HSC, as the target region of HSC is overlapped with the survey region of the SDSS-III BOSS.

An imperfect photometric redshift estimate from limited color information may result in a leakage of foreground galaxies to the source galaxy sample. This contamination not only dilutes the shear signals particularly near the cluster centers, but also complicates the self-calibration of the mean source redshift because such contamination cannot be described by a single parameter. This is a potentially important effect which should be studied carefully using mock catalogs or simulations.

One may consider that the photo- z outliers to cluster redshifts can be to some extent monitored by using an angular cross-correlation method of the source galaxy population with objects with spectroscopic redshifts or secure photo- z estimates, such as cluster themselves or spectroscopic LRG samples (e.g., [34, 92] for a study of the cross-correlation method). However, the cross-correlation method to eliminate the photo- z outliers may be limited by the magnification bias, as discussed below. First, lensing due to the foreground mass distribution causes the area of a given patch on the sky to increase, and thus diluting the number density of background galaxies. Second, galaxies fainter than the limiting magnitude can be magnified to cross the threshold. Therefore, if the magnitude cut is used in selecting source galaxies in addition to their colors, the magni-

fication bias may cause the observed densities of background galaxies to be increased or decreased, depending on the slope of the galaxy number counts. This magnification bias causes an apparent correlation between the densities of background galaxies and the cluster distribution (e.g., [86]), and hence degrades the power of the cross-correlation method. Here we give a rough estimate on the effect. The apparent cross-correlation between clusters of redshift slice z_l and the source galaxy distribution is given as $\langle n_{\text{gal}}(z_s)n_{\text{cl}}(z_l) \rangle \propto (2-5s)(\Delta z/H(z_l))W^\kappa(z_l)b_h(M)\xi_m(z_l)$ (see Eq. 18), where ξ_m is the mass correlation function of the cluster redshift z_l and s is the slope of the galaxy number count as a function of the galaxy magnitude m , i.e., $s \equiv d \ln n_{\text{gal}}/d \ln m$. On the other hand, a cross-correlation between (the outliers of) source galaxies and the cluster distribution is given as $\langle n_{\text{gal}}^{\text{photo-}z}(z_s)n_{\text{cl}}(z_l) \rangle \propto f_{\text{outlier}}(z_l)\Delta z b_h(M)b_g\xi_m(z_l)$, where $f_{\text{outlier}}(z_l)$ is the fraction of photo- z outliers leaking into the cluster redshift z_l . Hence the ratio of these cross-correlations can be found to be $O(0.1)/f_{\text{outlier}}$ for $z_l \sim 0.5$, assuming $b_g \sim 1$ and the magnitude slope $(2-5s) \sim 1$ as implied from observations [86]. Thus the cross-correlation method can eliminate photo- z outliers if the outliers contribute to the source galaxy catalog by more than 10% in a given cluster redshift slice. This rough estimate suggests that the cross-correlation method may not be so useful to perfectly eliminate the photo- z outliers. Even if this is the case, the shear and the magnification bias arise from the same mass distribution around the clusters, and therefore this magnification bias effect on the source galaxy population may be iteratively calibrated by combining the measurements of the stacked shear profile and the cross-correlation function. More optimistically, we may be able to improve the mass calibration with stacked lensing by adding information from the magnification bias (e.g., [93, 94]).

We note that the intrinsic alignments of galaxy ellipticities, which are a significant source of systematic errors for cosmic shear measurements (e.g., [60]), are not important for our analysis. This is because the stacked lensing is linear in shear, and does not include any correlation between the shapes of different galaxies.

The shape measurement of faint galaxies involves several uncertainties as extensively studied in the literature

(e.g., [95]). For the cosmic shear measured from upcoming wide-field surveys, the uncertainties such as the additive bias and multiplicative errors in the shear estimates need to be calibrated to better than 1% or 0.1% in shear in order not to significantly degrade cosmological parameter estimations [35]. Since our method focuses on the single population of source galaxies, all clusters share the same systematic errors in the shear calibrations, even if they exist, in such a way that they are uncorrelated with the distribution of foreground clusters. In this sense, this effect is similar to the source redshift uncertainty, especially for the multiplicative shear error. Thus we expect that the shape measurement errors can similarly be self-calibrated to the comparable accuracy to that of the source redshift uncertainty by using our method.

In this paper we assume the Gaussian statistics in computing the covariance of stacked weak lensing signal. The assumption is valid for the 1-halo term because one of the points is always fixed to the cluster center. On the other hand, the 2-halo term dominates only at very large scales, $\ell \lesssim 10^2$ (see Fig. 7), where the effect of the non-Gaussian error is small. Thus we expect the effect of non-Gaussian errors is small for our results. We also ignored the cross-covariance between the cluster number counts and the cluster power spectra (the 2-halo term and cluster-cluster angular power spectra). [59] has shown that the cross-correlation coefficients peak around $\ell \sim 10^3$, whereas in our calculations the information from the power spectra comes mainly from $\ell \sim 10^2$ (see Figs. 7 and 5). Therefore, the effect of the cross-covariance should also be small in our case.

Our results are based on the flat-sky and Limber's approximations. While the full calculation without relying on these approximations is not difficult [61], their effects on our results, i.e. forecast constraints on cosmological parameters, are expected to be small, because we are interested in sensitivities of the signals, rather than signals themselves, on cosmological parameters. An exception is constraints on the primordial non-Gaussianity, f_{NL} , as the constraints come mostly from very large scales ($\ell \sim \mathcal{O}(1)$) where these approximations obviously break down. Therefore, our results on f_{NL} should be taken with caution.

Also important are the effects of theoretical uncertainties, such as the inaccuracy of the halo mass function, the halo bias, and the radial profile. Previous work [96, 97] has found that theoretical uncertainties of the mass function and the halo bias can indeed be important. Such uncertainties might also be self-calibrated to some extent from the combination of observables studied in this paper, but the detailed exploration is beyond the scope of this paper.

There are several additional systematics in cluster weak lensing studies, including the effects of central galaxies, non-weak shear and magnification bias. Some of these effects on stacked cluster weak lensing have been investigated by [84]. Again, our conservative choice of $\ell_{\text{max}} = 10^4$ is meant to reduce these effects, but in prac-

tical analysis more careful treatments will be needed to minimize such effects, as done recently by [37].

VII. CONCLUSION

In this paper, we have estimated accuracies on cosmological parameters derivable from a joint experiment of the cluster observables (number counts and cluster-cluster correlation functions) and stacked weak lensing signals of distant galaxy shapes produced by the clusters, both of which can be drawn from a wide-field optical imaging survey. A striking advantage of this method is the derived cosmological constraints become insensitive to various systematic errors such as the source redshift uncertainty and the cluster mass-observable relation. Our key assumption to overcome these systematic uncertainties is to focus on a single population of background source galaxies to extract lensing signals around cluster at different redshifts. By cross-correlating the source galaxy shapes with the distribution of clusters with known redshifts (or at least secure photo- z estimates), we can statistically separate out the contribution at a given redshift slice from the total shear signals of the source galaxies. Put another way, this method enables a tomographic reconstruction of lensing structures. Moreover, the systematic errors of the cluster observables and the stacked lensing are closely related with each other, which enables an efficient self-calibration of these systematics (see Fig. 1 for the conceptual flow-chart). Specifically, the stacked lensing provides direct measurements of the mean mass of clusters, and therefore allows to calibrate the cluster mass-observable relation, whereas we can calibrate the source redshift uncertainty via the relative strengths of the stacked lensing signals at different cluster redshifts, because the stacked lensing signals at different cluster redshifts share the same source redshift uncertainty (*only if* the single population of background source galaxies is used, as assumed in this paper). As a result, cosmological parameters including dark energy parameters are well constrained yet least affected by these significant systematic effects (see Tables III and IV and Figs. 10, 13 and 14).

To estimate the cosmological power of the method above, we have developed a formulation to compute all the observables based on the halo model, and also derived the power spectra of the relevant correlation functions. In particular we have shown that the halo off-centering effect on the stacked lensing signals is expressed by a simple analytic form in Fourier space (see Appendix A). Moreover, the Fourier-space analysis greatly simplifies the Fisher matrix calculations, because the power spectrum covariances have the simpler forms than in real space. However, note that, even if the real-space observables such as the angular correlation functions are used as done in the previous measurements, the cosmological power should be equivalent to what was shown in this paper, because the two-point correlations and the

power spectra contain the equivalent information at two-point level. We believe that the formulation developed in this paper is useful in further extending the method, e.g., including additional power spectrum information such as the SZ power spectrum available from the upcoming wide-field SZ surveys with an overlap with optical imaging surveys, such as the HSC and the ACT or the DES and the SPT. The additional information can further improve the cosmological constraints, although new systematic errors introduced by new observations should carefully be studied. This is our future project, and will be presented elsewhere.

The results shown in this paper can be compared with the previous work studying the self-calibration technique for cluster observables, where the number counts and the cluster clustering information are combined to self-calibrate the mass-observable relation (e.g., [38]). We have found that adding the stacked lensing signals significantly improves the marginalized errors on each cosmological parameter by up to a factor of ~ 2 , especially the dark energy FoM by a factor of ~ 4 , which is achieved without assuming any priors on a number of nuisance parameters to model various systematic errors, including the mass-observable relation, the mean source galaxy redshift, offsets of cluster centers, and concentration parameters. The expected constraints on dark energy are quite comparable to those obtained from tomographic cosmic shear measurements obtained without including any systematic errors. We have shown that an accurate self-calibration of these systematic errors is indeed attained, with the mean source redshift calibrated to $\sigma(z_m) \sim 0.1$ and the mean cluster mass in each bin to $\sigma(\ln M_{\text{bias}}) \sim 0.05 - 0.1$ (see Fig. 11). We have also confirmed that clustering of massive clusters is powerful in constraining primordial non-Gaussianity. The robust constraint of $\sigma(f_{\text{NL}}) \lesssim 10$ can be obtained if the joint experiment is applied to upcoming imaging surveys.

In summary, we have demonstrated that weak lensing information and cluster observables, both available from the same imaging survey data, are complementary to each other. The cosmological power is greatly improved and an efficient self-calibration of various systematic uncertainties can be attained when the two measurements are combined. This is particularly promising given that there are several planned wide-field optical imaging surveys overlapping with SZ surveys: Subaru HSC survey and ACT, the DES and the SPT, and also the all-sky Planck CMB survey which will be available in a few years.

Acknowledgments

We thank D. Huterer, K. Ichiki, B. Jain and R. Mandelbaum for useful discussions. This work is supported in part by JSPS Core-to-Core Program “International Research Network for Dark Energy” and World Premier International Research Center Initiative (WPI Initiative), MEXT, Japan.

Appendix A: Derivation of Off-centered Lensing Signals

We consider an azimuthally averaged convergence profile, whose true center is located at θ_0 , at distance θ from the coordinate origin. It is expressed as

$$\begin{aligned}\kappa_{\text{off}}(\theta) &= \int \frac{d\phi'}{2\pi} \kappa(\theta' - \theta_0) \\ &= \int d^2\theta' \kappa(\theta' - \theta_0) W_\theta(\theta'),\end{aligned}\quad (\text{A1})$$

where $W_\theta(\theta')$ is defined by

$$W_\theta(\theta') \equiv \frac{1}{2\pi|\theta'|} \delta(|\theta'| - \theta). \quad (\text{A2})$$

The Fourier transform in angular space is given by

$$\begin{aligned}\tilde{\kappa}_{M,\text{off}}(\ell) &= \int d^2\theta e^{-i\ell\theta} \int d^2\theta' \kappa(\theta' - \theta_0) W_\theta(\theta'), \\ &= \int d^2\theta' J_0(\ell\theta') \int \frac{d^2\ell'}{(2\pi)^2} \tilde{\kappa}_M(\ell') e^{i\ell'(\theta' - \theta_0)} \\ &= \int \frac{d^2\ell'}{2\pi} \tilde{\kappa}_M(\ell') e^{-i\ell'\theta_0} \int \theta' d\theta' J_0(\ell\theta') J_0(\ell'\theta') \\ &= \int d\ell' \tilde{\kappa}_M(\ell') J_0(\ell'\theta_{\text{off}}) \delta(\ell - \ell') \\ &= \tilde{\kappa}_M(\ell) J_0(\ell\theta_{\text{off}}),\end{aligned}\quad (\text{A3})$$

where $\theta_{\text{off}} = |\theta_0|$, and used the integral representation of the Bessel function

$$J_0(x) = \int_0^{2\pi} \frac{d\phi}{2\pi} e^{ix \cos \phi}, \quad (\text{A4})$$

and the closure equation

$$\int_0^\infty x dx J_0(ax) J_0(bx) = \frac{1}{a} \delta(a - b). \quad (\text{A5})$$

Therefore the effect of off-centering is simply expressed as the multiplication of the zeroth order Bessel function in Fourier space. Note that Eq. (A3) is general expression applicable to any convergence profile κ . For reference, adopting the flat sky approximation convergence profiles $\kappa(\theta)$ and tangential shear profile $\gamma_+(\theta)$ with the effect of the offset are given by

$$\kappa(\theta) = \int \frac{\ell d\ell}{2\pi} \tilde{\kappa}_{M,\text{off}}(\ell) J_0(\ell\theta), \quad (\text{A6})$$

$$\gamma_+(\theta) = \int \frac{\ell d\ell}{2\pi} \tilde{\kappa}_{M,\text{off}}(\ell) J_2(\ell\theta). \quad (\text{A7})$$

In Fig. 16, we show the effect of off-centering on convergence and tangential shear profiles. Basically the effect is such that it flattens the convergence profile, and eliminates the tangential shear signals, below the offset size.

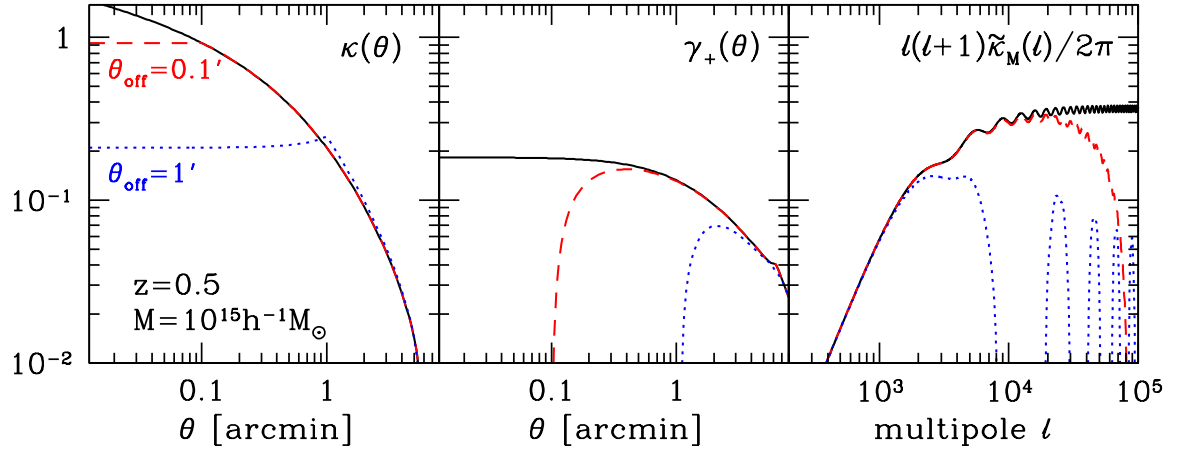


FIG. 16: Effect of off-centering on radial profiles of a single cluster with $M = 10^{15} h^{-1} M_{\odot}$ and $z = 0.5$, computed using the Fourier space description derived in Eq. (A3). From left to right panels, we show the convergence profile, the tangential shear profile, and the Fourier transform of the convergence. Solid lines show the case with no offset ($\theta_{\text{off}} = 0$), whereas dashed and dotted lines indicate profiles with the offset $\theta_{\text{off}} = 0.1'$ and $1'$, respectively.

Symbol	Definition	Eq.
$P_m^L(k)$	Linear mass power spectrum	(8)
$P_m^{\text{NL}}(k)$	Nonlinear mass power spectrum	(20)
M	Halo mass	(9)
M_{obs}	Cluster mass observable	(9)
$\sigma_{\ln M}$	Variance in mass-observable rel.	(9)
M_{bias}	Halo mass bias	(9)
$z_{i,\text{min}}, z_{i,\text{max}}$	The i -th redshift bin of clusters	(11)
$M_{b,\text{min}}, M_{b,\text{max}}$	The b -th mass bin of clusters	(11)
$n_{i(b)}, N_{i(b)}$	Cluster number counts	(11), (13)
dn/dM	Halo mass function	(11)
$S_{i(b)}(M)$	Selection function of clusters	(12)
$C_{i(bb')}^{\text{hh}}(\ell)$	Cluster power spectrum	(14)
$W_{i(b)}^h(M)$	Weight function of clusters	(15)
$b_h(M)$	Halo bias	(15)
$W^{\kappa}(z)$	Lensing weight function	(19)
$C^{\kappa\kappa}(\ell)$	Shear power spectrum	(20)
$\langle \gamma_+ \rangle_{i(b)}(\theta)$	Tangential shear profile	(22)
$C_{i(b)}^{\text{h}\kappa}(\ell)$	Shear-cluster power spectrum	(36)
$C_{i(b)}^{\text{h}\kappa, 1\text{h}}(\ell)$	1-halo term of $C^{\text{h}\kappa}(\ell)$	(27)
$C_{i(b)}^{\text{h}\kappa, 2\text{h}}(\ell)$	2-halo term of $C^{\text{h}\kappa}(\ell)$	(35)
$\tilde{u}_M(k)$	Halo mass profile	(29)
$\tilde{\kappa}_M(\ell)$	Halo convergence profile	(28)
$\tilde{\kappa}_{M,\text{off}}(\ell)$	With halo centering offset	(34)
$c(M, z)$	Halo concentration	(26)

TABLE VI: Symbols used in the paper.

Appendix B: Summary of Symbols

In Table VI we give a summary of symbols commonly used in the paper.

[1] A. Albrecht, G. Bernstein, R. Cahn, W. L. Freedman, J. Hewitt, W. Hu, J. Huth, M. Kamionkowski, E. W.

Kolb, L. Knox, et al., ArXiv Astrophysics e-prints (2006), arXiv:astro-ph/0609591.

- [2] A. Vikhlinin, A. V. Kravtsov, R. A. Burenin, H. Ebeling, W. R. Forman, A. Hornstrup, C. Jones, S. S. Murray, D. Nagai, H. Quintana, et al., *Astrophys. J.* **692**, 1060 (2009), 0812.2720.
- [3] A. Mantz, S. W. Allen, D. Rapetti, and H. Ebeling, *Mon. Not. Roy. Astron. Soc.* **406**, 1759 (2010), 0909.3098.
- [4] E. Rozo, R. H. Wechsler, E. S. Rykoff, J. T. Annis, M. R. Becker, A. E. Evrard, J. A. Frieman, S. M. Hansen, J. Hao, D. E. Johnston, et al., *Astrophys. J.* **708**, 645 (2010), 0902.3702.
- [5] R. Reyes, R. Mandelbaum, U. Seljak, T. Baldauf, J. E. Gunn, L. Lombriser, and R. E. Smith, *Nature (London)* **464**, 256 (2010), 1003.2185.
- [6] F. Schmidt, A. Vikhlinin, and W. Hu, *Phys. Rev. D* **80**, 083505 (2009), 0908.2457.
- [7] D. Rapetti, S. W. Allen, A. Mantz, and H. Ebeling, *Mon. Not. Roy. Astron. Soc.* **406**, 1796 (2010), 0911.1787.
- [8] N. Dalal, O. Doré, D. Huterer, and A. Shirokov, *Phys. Rev. D* **77**, 123514 (2008), arXiv:0710.4560.
- [9] M. Oguri, *Physical Review Letters* **102**, 211301 (2009), 0905.0920.
- [10] M. Roncarelli, L. Moscardini, E. Branchini, K. Dolag, M. Grossi, F. Iannuzzi, and S. Matarrese, *Mon. Not. Roy. Astron. Soc.* **402**, 923 (2010), 0909.4714.
- [11] C. Cunha, D. Huterer, and O. Doré, *Phys. Rev. D* **82**, 023004 (2010), 1003.2416.
- [12] B. Sartoris, S. Borgani, C. Fedeli, S. Matarrese, L. Moscardini, P. Rosati, and J. Weller, *Mon. Not. Roy. Astron. Soc.* **407**, 2339 (2010), 1003.0841.
- [13] A. Mantz, S. W. Allen, H. Ebeling, and D. Rapetti, *Mon. Not. Roy. Astron. Soc.* **387**, 1179 (2008), 0709.4294.
- [14] T. H. Reiprich and H. Böhringer, *Astrophys. J.* **567**, 716 (2002), arXiv:astro-ph/0111285.
- [15] E. S. Rykoff, A. E. Evrard, T. A. McKay, M. R. Becker, D. E. Johnston, B. P. Koester, B. Nord, E. Rozo, E. S. Sheldon, R. Stanek, et al., *Mon. Not. Roy. Astron. Soc.* **387**, L28 (2008), 0802.1069.
- [16] A. Finoguenov, T. H. Reiprich, and H. Böhringer, *Astron. Astrophys.* **368**, 749 (2001), arXiv:astro-ph/0010190.
- [17] M. Shimizu, T. Kitayama, S. Sasaki, and Y. Suto, *Astrophys. J.* **590**, 197 (2003), arXiv:astro-ph/0212284.
- [18] A. J. R. Sanderson, T. J. Ponman, A. Finoguenov, E. J. Lloyd-Davies, and M. Markevitch, *Mon. Not. Roy. Astron. Soc.* **340**, 989 (2003), arXiv:astro-ph/0301049.
- [19] M. Arnaud, E. Pointecouteau, and G. W. Pratt, *Astron. Astrophys.* **441**, 893 (2005), arXiv:astro-ph/0502210.
- [20] N. Okabe, M. Takada, K. Umetsu, T. Futamase, and G. P. Smith, *Publ. Astron. Soc. Japan* **62**, 811 (2010), 0903.1103.
- [21] D. E. Johnston, E. S. Sheldon, R. H. Wechsler, E. Rozo, B. P. Koester, J. A. Frieman, T. A. McKay, A. E. Evrard, M. R. Becker, and J. Annis, *ArXiv e-prints* (2007), 0709.1159.
- [22] M. Bonamente, M. Joy, S. J. LaRoque, J. E. Carlstrom, D. Nagai, and D. P. Marrone, *Astrophys. J.* **675**, 106 (2008), 0708.0815.
- [23] D. P. Marrone, G. P. Smith, J. Richard, M. Joy, M. Bonamente, N. Hasler, V. Hamilton-Morris, J. Kneib, T. Culverhouse, J. E. Carlstrom, et al., *Astrophys. J.* **701**, L114 (2009), 0907.1687.
- [24] A. V. Kravtsov, A. Vikhlinin, and D. Nagai, *Astrophys. J.* **650**, 128 (2006), arXiv:astro-ph/0603205.
- [25] Y. Zhang, A. Finoguenov, H. Böhringer, J. Kneib, G. P. Smith, R. Kneissl, N. Okabe, and H. Dahle, *Astron. Astrophys.* **482**, 451 (2008), 0802.0770.
- [26] A. Mantz, S. W. Allen, H. Ebeling, D. Rapetti, and A. Drlica-Wagner, *Mon. Not. Roy. Astron. Soc.* **406**, 1773 (2010), 0909.3099.
- [27] M. Bartelmann and P. Schneider, *Phys. Rep.* **340**, 291 (2001), arXiv:astro-ph/9912508.
- [28] P. Fischer, T. A. McKay, E. Sheldon, A. Connolly, A. Stebbins, J. A. Frieman, B. Jain, M. Joffre, D. Johnston, G. Bernstein, et al., *Astron. J.* **120**, 1198 (2000), arXiv:astro-ph/9912119.
- [29] T. A. McKay, E. S. Sheldon, J. Racusin, P. Fischer, U. Seljak, A. Stebbins, D. Johnston, J. A. Frieman, N. Bahcall, J. Brinkmann, et al., *ArXiv Astrophysics e-prints* (2001), arXiv:astro-ph/0108013.
- [30] E. S. Sheldon, J. Annis, H. Böhringer, P. Fischer, J. A. Frieman, M. Joffre, D. Johnston, T. A. McKay, C. Miller, R. C. Nichol, et al., *Astrophys. J.* **554**, 881 (2001), arXiv:astro-ph/0103029.
- [31] J. Guzik and U. Seljak, *Mon. Not. Roy. Astron. Soc.* **321**, 439 (2001), arXiv:astro-ph/0007067.
- [32] E. S. Sheldon, D. E. Johnston, R. Scranton, B. P. Koester, T. A. McKay, H. Oyaizu, C. Cunha, M. Lima, H. Lin, J. A. Frieman, et al., *Astrophys. J.* **703**, 2217 (2009), 0709.1153.
- [33] R. Mandelbaum, A. Tasitsiomi, U. Seljak, A. V. Kravtsov, and R. H. Wechsler, *Mon. Not. Roy. Astron. Soc.* **362**, 1451 (2005), arXiv:astro-ph/0410711.
- [34] A. J. Nishizawa, M. Takada, T. Hamana, and H. Furusawa, *Astrophys. J.* **718**, 1252 (2010), 1002.2476.
- [35] D. Huterer, M. Takada, G. Bernstein, and B. Jain, *Mon. Not. Roy. Astron. Soc.* **366**, 101 (2006), arXiv:astro-ph/0506030.
- [36] A. P. Hearin, A. R. Zentner, Z. Ma, and D. Huterer, *Astrophys. J.* **720**, 1351 (2010), 1002.3383.
- [37] R. Mandelbaum, U. Seljak, T. Baldauf, and R. E. Smith, *Mon. Not. Roy. Astron. Soc.* **405**, 2078 (2010), 0911.4972.
- [38] S. Majumdar and J. J. Mohr, *Astrophys. J.* **613**, 41 (2004), arXiv:astro-ph/0305341.
- [39] M. Lima and W. Hu, *Phys. Rev. D* **70**, 043504 (2004), arXiv:astro-ph/0401559.
- [40] M. Lima and W. Hu, *Phys. Rev. D* **72**, 043006 (2005), arXiv:astro-ph/0503363.
- [41] S. Miyazaki, Y. Komiyama, H. Nakaya, Y. Doi, H. Furusawa, P. Gillingham, Y. Kamata, K. Takeshi, and K. Narai, in *Society of Photo-Optical Instrumentation Engineers (SPIE) Conference Series* (2006), vol. 6269 of *Society of Photo-Optical Instrumentation Engineers (SPIE) Conference Series*.
- [42] The Dark Energy Survey Collaboration, *ArXiv Astrophysics e-prints* (2005), arXiv:astro-ph/0510346.
- [43] LSST Science Collaborations, P. A. Abell, J. Allison, S. F. Anderson, J. R. Andrew, J. R. P. Angel, L. Armus, D. Arnett, S. J. Asztalos, T. S. Axelrod, et al., *ArXiv e-prints* (2009), 0912.0201.
- [44] A. D. Hincks, V. Acquaviva, P. Ade, P. Aguirre, M. Amiri, J. W. Appel, L. F. Barrientos, E. S. Battistelli, J. R. Bond, B. Brown, et al., *ArXiv e-prints* (2009), 0907.0461.
- [45] M. D. Niemack, P. A. R. Ade, J. Aguirre, F. Barrientos, J. A. Beall, J. R. Bond, J. Britton, H. M. Cho, S. Das, M. J. Devlin, et al., *ArXiv e-prints* (2010), 1006.5049.

- [46] K. Vanderlinde, T. M. Crawford, T. de Haan, J. P. Dudley, L. Shaw, P. A. R. Ade, K. A. Aird, B. A. Benson, L. E. Bleem, M. Brodwin, et al., ArXiv e-prints (2010), 1003.0003.
- [47] E. Komatsu, K. M. Smith, J. Dunkley, C. L. Bennett, B. Gold, G. Hinshaw, N. Jarosik, D. Larson, M. R. Nolta, L. Page, et al., ArXiv e-prints (2010), 1001.4538.
- [48] M. Takada and B. Jain, Mon. Not. Roy. Astron. Soc. **348**, 897 (2004), arXiv:astro-ph/0310125.
- [49] W. Hu, Astrophys. J. **522**, L21 (1999), arXiv:astro-ph/9904153.
- [50] D. Huterer, Phys. Rev. D **65**, 063001 (2002), arXiv:astro-ph/0106399.
- [51] L. Wang and P. J. Steinhardt, Astrophys. J. **508**, 483 (1998), arXiv:astro-ph/9804015.
- [52] M. Takada, E. Komatsu, and T. Futamase, Phys. Rev. D **73**, 083520 (2006), arXiv:astro-ph/0512374.
- [53] D. J. Eisenstein and W. Hu, Astrophys. J. **496**, 605 (1998), arXiv:astro-ph/9709112.
- [54] E. Komatsu, J. Dunkley, M. R. Nolta, C. L. Bennett, B. Gold, G. Hinshaw, N. Jarosik, D. Larson, M. Limon, L. Page, et al., Astrophys. J. Suppl. **180**, 330 (2009), arXiv:0803.0547.
- [55] S. Bhattacharya, K. Heitmann, M. White, Z. Lukić, C. Wagner, and S. Habib, ArXiv e-prints (2010), 1005.2239.
- [56] D. N. Limber, Astrophys. J. **119**, 655 (1954).
- [57] M. Lo Verde, A. Miller, S. Shandera, and L. Verde, JCAP **4**, 14 (2008), 0711.4126.
- [58] R. E. Smith, J. A. Peacock, A. Jenkins, S. D. M. White, C. S. Frenk, F. R. Pearce, P. A. Thomas, G. Efstathiou, and H. M. P. Couchman, Mon. Not. Roy. Astron. Soc. **341**, 1311 (2003), arXiv:astro-ph/0207664.
- [59] M. Takada and S. Bridle, New Journal of Physics **9**, 446 (2007), arXiv:0705.0163.
- [60] C. M. Hirata and U. Seljak, Phys. Rev. D **70**, 063526 (2004), arXiv:astro-ph/0406275.
- [61] R. de Putter and M. Takada, ArXiv e-prints (2010), 1007.4809.
- [62] J. F. Navarro, C. S. Frenk, and S. D. M. White, Astrophys. J. **490**, 493 (1997), arXiv:astro-ph/9611107.
- [63] T. T. Nakamura and Y. Suto, Progress of Theoretical Physics **97**, 49 (1997), arXiv:astro-ph/9612074.
- [64] J. S. Bullock, T. S. Kolatt, Y. Sigad, R. S. Somerville, A. V. Kravtsov, A. A. Klypin, J. R. Primack, and A. Dekel, Mon. Not. Roy. Astron. Soc. **321**, 559 (2001), arXiv:astro-ph/9908159.
- [65] A. R. Duffy, J. Schaye, S. T. Kay, and C. Dalla Vecchia, Mon. Not. Roy. Astron. Soc. **390**, L64 (2008), 0804.2486.
- [66] R. Scoccimarro, R. K. Sheth, L. Hui, and B. Jain, Astrophys. J. **546**, 20 (2001), arXiv:astro-ph/0006319.
- [67] M. Takada and B. Jain, Mon. Not. Roy. Astron. Soc. **340**, 580 (2003), arXiv:astro-ph/0209167.
- [68] M. Oguri, M. Takada, N. Okabe, and G. P. Smith, Mon. Not. Roy. Astron. Soc. **405**, 2215 (2010), 1004.4214.
- [69] S. Hilbert and S. D. M. White, Mon. Not. Roy. Astron. Soc. **404**, 486 (2010), 0907.4371.
- [70] Y. Lin and J. J. Mohr, Astrophys. J. **617**, 879 (2004), arXiv:astro-ph/0408557.
- [71] B. P. Koester, T. A. McKay, J. Annis, R. H. Wechsler, A. Evrard, L. Bleem, M. Becker, D. Johnston, E. Sheldon, R. Nichol, et al., Astrophys. J. **660**, 239 (2007), arXiv:astro-ph/0701265.
- [72] H. Shan, B. Qin, B. Fort, C. Tao, X. Wu, and H. Zhao, Mon. Not. Roy. Astron. Soc. **406**, 1134 (2010), 1004.1475.
- [73] W. Hu and A. V. Kravtsov, Astrophys. J. **584**, 702 (2003), arXiv:astro-ph/0203169.
- [74] M. Takada and B. Jain, Mon. Not. Roy. Astron. Soc. **395**, 2065 (2009), 0810.4170.
- [75] M. Sato, T. Hamana, R. Takahashi, M. Takada, N. Yoshida, T. Matsubara, and N. Sugiyama, Astrophys. J. **701**, 945 (2009), 0906.2237.
- [76] H. Hoekstra, Mon. Not. Roy. Astron. Soc. **339**, 1155 (2003), arXiv:astro-ph/0208351.
- [77] S. Dodelson, Phys. Rev. D **70**, 023008 (2004), arXiv:astro-ph/0309277.
- [78] D. Jeong, E. Komatsu, and B. Jain, Phys. Rev. D **80**, 123527 (2009), 0910.1361.
- [79] M. Sato, M. Takada, T. Hamana, and T. Matsubara, ArXiv e-prints (2010), 1009.2558.
- [80] A. Lewis, A. Challinor, and A. Lasenby, Astrophys. J. **538**, 473 (2000), arXiv:astro-ph/9911177.
- [81] U. Seljak and M. Zaldarriaga, Astrophys. J. **469**, 437 (1996), arXiv:astro-ph/9603033.
- [82] D. J. Eisenstein, I. Zehavi, D. W. Hogg, R. Scoccimarro, M. R. Blanton, R. C. Nichol, R. Scranton, H. Seo, M. Tegmark, Z. Zheng, et al., Astrophys. J. **633**, 560 (2005), arXiv:astro-ph/0501171.
- [83] H. Seo and D. J. Eisenstein, Astrophys. J. **598**, 720 (2003), arXiv:astro-ph/0307460.
- [84] E. Rozo, H. Wu, and F. Schmidt, ArXiv e-prints (2010), 1009.0756.
- [85] R. Mandelbaum, U. Seljak, and C. M. Hirata, JCAP **8**, 6 (2008), 0805.2552.
- [86] T. Broadhurst, M. Takada, K. Umetsu, X. Kong, N. Arimoto, M. Chiba, and T. Futamase, Astrophys. J. **619**, L143 (2005), arXiv:astro-ph/0412192.
- [87] T. Broadhurst, K. Umetsu, E. Medezinski, M. Oguri, and Y. Rephaeli, Astrophys. J. **685**, L9 (2008), 0805.2617.
- [88] M. Oguri, J. F. Hennawi, M. D. Gladders, H. Dahle, P. Natarajan, N. Dalal, B. P. Koester, K. Sharon, and M. Bayliss, Astrophys. J. **699**, 1038 (2009), 0901.4372.
- [89] N. Okabe, Y. Zhang, A. Finoguenov, M. Takada, G. P. Smith, K. Umetsu, and T. Futamase, Astrophys. J. **721**, 875 (2010), 1007.3816.
- [90] M. Lima and W. Hu, Phys. Rev. D **76**, 123013 (2007), 0709.2871.
- [91] H. Lin, M. Lima, H. Oyaizu, C. Cunha, J. Frieman, J. Annis, B. Koester, J. Hao, T. McKay, and E. Sheldon, in *Bulletin of the American Astronomical Society* (2006), vol. 38 of *Bulletin of the American Astronomical Society*, pp. 1196–+.
- [92] J. A. Newman, Astrophys. J. **684**, 88 (2008), 0805.1409.
- [93] L. Van Waerbeke, H. Hildebrandt, J. Ford, and M. Mileraitis, ArXiv e-prints (2010), 1004.3793.
- [94] E. Rozo and F. Schmidt, ArXiv e-prints (2010), 1009.5735.
- [95] S. Bridle, S. T. Balan, M. Bethge, M. Gentile, S. Harmeling, C. Heymans, M. Hirsch, R. Hosseini, M. Jarvis, D. Kirk, et al., Mon. Not. Roy. Astron. Soc. **405**, 2044 (2010), 0908.0945.
- [96] C. E. Cunha and A. E. Evrard, Phys. Rev. D **81**, 083509 (2010), 0908.0526.
- [97] H. Wu, A. R. Zentner, and R. H. Wechsler, Astrophys. J. **713**, 856 (2010), 0910.3668.
- [98] <http://www.sciops.esa.int/index.php?project=PLANCK>
- [99] <http://cosmology.lbl.gov/BOSS/>